Economic Geology, v. 115, no. 8, pp. 1619–1644

Occurrence and Distribution of Silver in the World-Class Río Blanco Porphyry Cu-Mo Deposit, Central Chile

Jorge Crespo,[1,2,†,*] Martin Reich,[1,2] Fernando Barra,[1,2] Juan José Verdugo,[3] Claudio Martínez,[3] Mathieu Leisen,[1,2] Rurik Romero,[1,2] Diego Morata,[1,2] and Carlos Marquardt[4]

[1]*Department of Geology and Andean Geothermal Center of Excellence (CEGA), Facultad de Ciencias Físicas y Matemáticas (FCFM), Universidad de Chile, Plaza Ercilla 803, Santiago 8370450, Chile*

[2]*Millennium Nucleus for Metal Tracing Along Subduction, Facultad de Ciencias Físicas y Matemáticas (FCFM), Universidad de Chile, Santiago 8370450, Chile*

[3]*CODELCO, División Andina, Avenida Santa Teresa, No. 513 Los Andes, V Región, Chile*

[4]*Department of Mining Engineering and Department of Structural and Geotechnical Engineering, Pontificia Universidad Católica de Chile, Av. Vicuña Mackenna 4860, Santiago 7820436, Chile*

Abstract

Porphyry Cu-Mo deposits (PCDs) are the world's major source of Cu, Mo, and Re and are also a significant source of Au and Ag. Here we focus on the world-class Río Blanco PCD in the Andes of central Chile, where Ag is a by-product of Cu mining. Statistical examination of an extensive multielemental inductively coupled plasma-mass spectrometry data set indicates compositional trends at the deposit scale, including Ag-Cu (r = 0.71) and Ag-In (r = 0.53) positive correlations, which relate to Cu-Fe sulfides and Cu sulfosalts in the deposit. Silver is primarily concentrated in Cu ores in the central core of the deposit, and significant variations in the Ag concentration are related to the different hydrothermal alteration types. The concentration of Ag is highest in the potassic core (avg 2.01 ppm) and decreases slightly in the gray-green sericite (phyllic) zone (avg 1.72 ppm); Ag is lowest in the outer propylitic alteration zone (avg 0.59 ppm). Drill core samples from major hydrothermal alteration zones were selected for in situ analysis of Ag and associated elements in sulfide and sulfosalt minerals. To ensure representativeness, sample selection considered the spatial distribution of the alteration types and ore paragenesis. Chalcopyrite is the most abundant Cu sulfide in Río Blanco, with Ag concentration that ranges from sub-parts per million levels to hundreds of parts per million. The highest concentration of Ag in chalcopyrite is associated with the high-temperature potassic alteration stage. Bornite is less abundant than chalcopyrite but has the highest Ag concentration of all studied sulfides, ranging from hundreds of parts per million up to ~1,000 ppm. The Ag concentration in bornite is higher in lower-temperature alteration assemblages (moderate gray-green sericite), opposite to the behavior of Ag in chalcopyrite. Pyrite has the lowest Ag content, although concentrations of other critical elements such as Co, Ni, and Au may be significant. The highest Ag concentrations, i.e., thousands of parts per million up to weight percent levels, were detected in late-stage Cu sulfosalts (enargite, tennantite, and tetrahedrite). The Ag content in these sulfosalts increases with increasing Sb concentrations, from the Sb-poor enargite to the Sb-rich tetrahedrite. The earliest Ag mineralization event is related to the potassic alteration stage represented by early biotite and transitional early biotite-type veinlets and where the predominant sulfides are chalcopyrite and bornite. Silver mineralization during this stage was predominantly controlled by crystallization of Cu-Fe sulfides. The second Ag mineralization event at Río Blanco is associated with the transitional Cu mineralization stage, which is represented by the gray-green sericite alteration (C-type veinlets). In this alteration type, Ag was partitioned preferentially into chalcopyrite, bornite, and to a lesser extent pyrite. The last Ag mineralization event is related to the late quartz-sericite alteration stage, characterized by D- and E-type veinlets with pyrite-chalcopyrite and enargite-tennantite-tetrahedrite. Our data indicate that Ag was associated with several Cu mineralization episodes at Río Blanco, with Ag concentration apparently controlled by cooling, changes in pH, fO_2 and fS_2 of the hydrothermal fluids, and the intensity of alteration. Overall, our results provide information on critical metal partitioning between sulfides, plus the distribution of critical element resources at the deposit scale. Knowledge of the mineralogical occurrence of critical metals in PCDs is necessary to better assess their resources and evaluate the potential for their recovery.

Introduction

Porphyry copper deposits (PCDs) are the world's major source of copper and molybdenum, and some also contain appreciable quantities of gold. Aside from Cu, Mo, and Au, significant amounts of other elements, such as Ag, Re, Se, Te, As, and Pd, are recovered from some PCDs (Singer et al., 2008; John and Taylor, 2016). Despite their low average concentrations in Cu ores (e.g., 100s of ppb to a few ppm), these trace elements are recovered as by-products of Cu mining of some PCDs. For example, ~80% of the Re and nearly all of the Te and Se are obtained from porphyry Cu deposits (John and Taylor, 2016). Most of these elements are considered as critical metals because they are both essential for modern society technological development and subject to the risk of supply restriction (U.S. Department of Energy, 2011; Geological Society of America, 2013; Arndt et al., 2017; Hayes and McCulloug, 2018). Therefore, considering the large number of PCDs worldwide and the volume of ore processed, these deposits are potential

[†]Corresponding author: e-mail, jorge.crespo@ug.uchile.cl
[*]Present address: Department of Mining Engineering, Colorado School of Mines, 1600 Illinois Street, Golden, Colorado 80401, USA.

ISSN 0361-0128; doi:10.5382/econgeo.4778; 26 p.
Digital appendices are available in the online Supplements section.

Submitted: October 18, 2019 / Accepted: April 20, 2020

sources for critical commodities including Co, In, Bi, Nb, U, rare earth elements (REEs), and platinum group elements (PGEs), among others (Economou-Eliopoulos and Eliopoulos, 1999; Tarkian and Stribrny, 1999; Economou-Eliopoulos, 2005; Pašava et al., 2010; Cioacâ et al., 2014; John and Taylor, 2016; McFall et al., 2018).

Among trace commodities, Au and Ag are typically significant by-products in PCDs. Gold grades in this deposit type range from 0.0011 to 1.3 g/t Au, with an estimated average of 0.276 g/t Au (Singer et al., 2008; John and Taylor, 2016). Previous studies have shown that Au in PCDs is preferentially incorporated into bornite and chalcopyrite within potassic alteration zones (Kesler et al., 2002; Arif and Baker, 2004). At the Skouries (Greece), Batu Hijau (Indonesia), and Kingking (Philippines) PCDs, bornite contains ~1 ppm Au, whereas chalcopyrite has about an order of magnitude less (Kesler et al., 2002). Arif and Baker (2004) reported similar Au values at Batu Hijau, where Au in bornite has distinctly higher concentrations compared to chalcopyrite (0.6–38.37 and 0.11–0.29 ppm, respectively). More recently, Cioacâ et al. (2014) reported even higher Au concentrations in chalcopyrite (up to 970 ppm) and pyrite (up to 256 ppm) in PCDs from Romania, where bornite can reach up to 920 ppm due to the presence of Au-bearing inclusions. On the other hand, pyrite can host significant amounts of Au (up to 700 ppm) as reported by Reich et al. (2013a) in the Dexing PCD in China. Gold in sulfides is present both as a structurally bound element, i.e., in solid solution, and forming micro- to nanosized particles or inclusions of native gold, electrum, or Au tellurides (e.g., Rubin and Kyle, 1997; Kesler et al., 2002; Arif and Baker, 2004; Palenik et al., 2004; Reich et al., 2005, 2006, 2013a; Deditius et al., 2011; Franchini et al., 2015; Crespo et al., 2018; Sykora et al., 2018).

Silver is commonly used in a wide range of applications. In addition to its historical use in the fabrication of coins, Ag currently has a strong industrial demand for numerous products, including solar panels, jewelry, silverware, bactericides, and pharmaceuticals, and new uses as batteries in flexible electronics and in the automotive industry (World Silver Survey, 2019). Although a portion of the Ag supply is associated with epithermal deposits and Pb-Zn mining, much Ag is obtained as a by-product from PCDs (U.S. Geological Survey, 2019; World Silver Survey, 2019). Silver grades reported by Singer et al. (2008) and John and Taylor (2016) for 172 PCDs range from 0.095 to 21 g/t with an average of ~2.90 g/t. Silver is present primarily in Cu-Au ± Mo ore zones in the central cores of porphyry systems, where it is thought to occur in solid solution in bornite and chalcopyrite (John and Taylor, 2016, and references therein); however, it can also be present in sphalerite, galena, argentite/acanthite, electrum, sulfosalts, and telluride minerals (e.g., Ballantyne et al., 1998; Arif and Baker, 2004; Singer et al., 2008). More recent studies using secondary ion mass spectrometry (SIMS) have reported Ag concentrations of up to approximately thousands of parts per million in bornite, chalcopyrite, and chalcocite in the Mantos Blancos porphyry-type Cu deposit in northern Chile (Reich et al., 2013b). Cioacâ et al. (2014) suggest that Ag in bornite and chalcopyrite from PCDs in Romania may reach concentrations up to 4,830 and 1,180 ppm, respectively, possibly due to the presence of Ag-bearing inclusions. In general, Ag in bornite is one order of magnitude higher than in chalcopyrite and two orders of magnitude higher than in pyrite for Romanian PCDs (Cioacâ et al., 2014). A reconnaissance study by Crespo et al. (2018) at the Río Blanco PCD in central Chile indicated that Ag occurs, at least in part, as Ag-bearing micro- to nanosized mineral inclusions in Cu-Fe sulfides in potassic and phyllic alteration zones.

Despite the economic significance of Ag, there have not been any systematic mineralogical and geochemical studies of Ag deportment in porphyry Cu systems. The distribution of Ag at the deposit scale and its genetic relationship to hydrothermal alteration and sulfide (and sulfosalt) assemblages is not known, even though such information is critical to understand the behavior of Ag in porphyry Cu systems and its relationship to Cu-Mo mineralization events. The distribution of Ag and other economically important commodities at the deposit scale is necessary for the resource assessment of critical elements and related geometallurgical studies.

This study provides data on the distribution of Ag in the supergiant Río Blanco deposit in central Chile, where Ag is extracted as a by-product from Cu sulfide ores. In order to constrain the occurrence and distribution of Ag at the Río Blanco deposit, we conducted a statistical examination of an extensive drill core geochemical inductively coupled plasma-mass spectrometry (ICP-MS) database (~10,000 data points), which pointed to major elemental trends at the deposit scale, including distinctive Cu-Ag, Ag-In, Ag-Se, and Ag-Bi trends. Based on the statistical analysis, representative drill core samples from all major hydrothermal types were then selected for in situ mineral studies. In order to attain high-resolution textural and compositional information, mineralogical observations and geochemical analyses used a combination of conventional and field emission-scanning electron microscopy (SEM and FE-SEM), electron microprobe analysis (EMPA), and laser ablation-inductively coupled plasma-mass spectrometry (LA-ICP-MS). To ensure that samples are representative, the spatial distribution of alteration and mineralization types plus sulfide paragenesis was considered. We show that Ag in Río Blanco displays a complex spatial distribution that correlates with the main alteration types and Cu-Mo mineralization events. Our data indicate that Ag is largely contained in sulfides and sulfosalts and at the deposit scale primarily occurs as a structurally bound metal in association mainly with Cu and In.

Geologic Background

Geology of the Río Blanco deposit

The Río Blanco-Los Bronces district in the high Andes of central Chile constitutes the world's largest known concentration of Cu with 206.7 million tonnes (Mt) (Toro et al., 2012; CODELCO, 2018). The Río Blanco-Los Bronces cluster comprises several mineralized centers aligned in a north-northwest orientation (Irarrazaval et al., 2010; Sillitoe, 2010; Mpodozis and Cornejo, 2012; Toro et al., 2012; Piquer et al., 2015, 2019; Yáñez and Rivera, 2019). The tectonic evolution of this Andean segment was influenced by regional-scale fault systems (NW- and NE-striking faults), oriented oblique to the north-south axis of the orogeny (Mpodozis and Cornejo, 2012; Piquer et al., 2015, 2019; Yáñez and Rivera, 2019). These faults were reactivated during the Mio-

Pliocene east-west contraction coeval with the deposition of the Farellones Formation and the emplacement of the Río Blanco-San Francisco batholith, whose final pulses were genetically linked to the formation of the Río Blanco ore deposit. Magmatic and hydrothermal fluid flow was channeled and focused by both sets of preexisting oblique structures, and, in turn, fault rupture was driven by high fluid pressures (Mpodozis and Cornejo, 2012; Piquer et al., 2015, 2019; Yáñez and Rivera, 2019).

The Río Blanco deposit, located in the high Andes at an altitude of 3,700 to 4,300 m above sea level (a.s.l.), is operated by CODELCO-Andina. In 2018, Andina produced 220,000 tons of fine copper with an estimated 20,000 kg of Ag as a by-product (CODELCO, 2018). Mining activities at Río Blanco are focused on three areas, i.e., the Río Blanco underground mine and the Don Luis and Sur-Sur open pits (Fig. 1). The geology of the Río Blanco porphyry deposit has been extensively described (Warnaars et al., 1985; Serrano et al., 1996; Vargas et al., 1999; Frikken, 2004; Hollings et al., 2005; Mpodozis and Cornejo, 2012; Toro et al., 2012; Piquer et al., 2015, 2019; Crespo et al., 2018). The oldest rocks at Río Blanco correspond to andesite lavas and stratified basaltic andesites of the Farellones Formation, with a U-Pb zircon age of 17.2 ± 0.05 Ma (Deckart et al., 2005). Reported K-Ar and U-Pb ages indicate that the intrusive activity in the Río Blanco-Los Bronces district was continuous through the early to middle Miocene and broadly coeval with the Farellones Formation volcanism (Warnaars et al., 1985; Deckart et al., 2005, 2013; Piquer et al., 2015, 2019). The Farellones Formation is intruded by the San Francisco batholith, which comprises several plutonic phases over an area of 200 km² (Thiele, 1980; Stambuk et al., 1982; Vergara and Latorre, 1984; Serrano et al., 1996). Deckart et al. (2005, 2013) reported U-Pb zircon ages for the three main intrusive phases of the San Francisco batholith—i.e., the Río Blanco granodiorite (11.96 ± 0.04 Ma), the Cascada granodiorite (8.40 ± 0.23 Ma), and

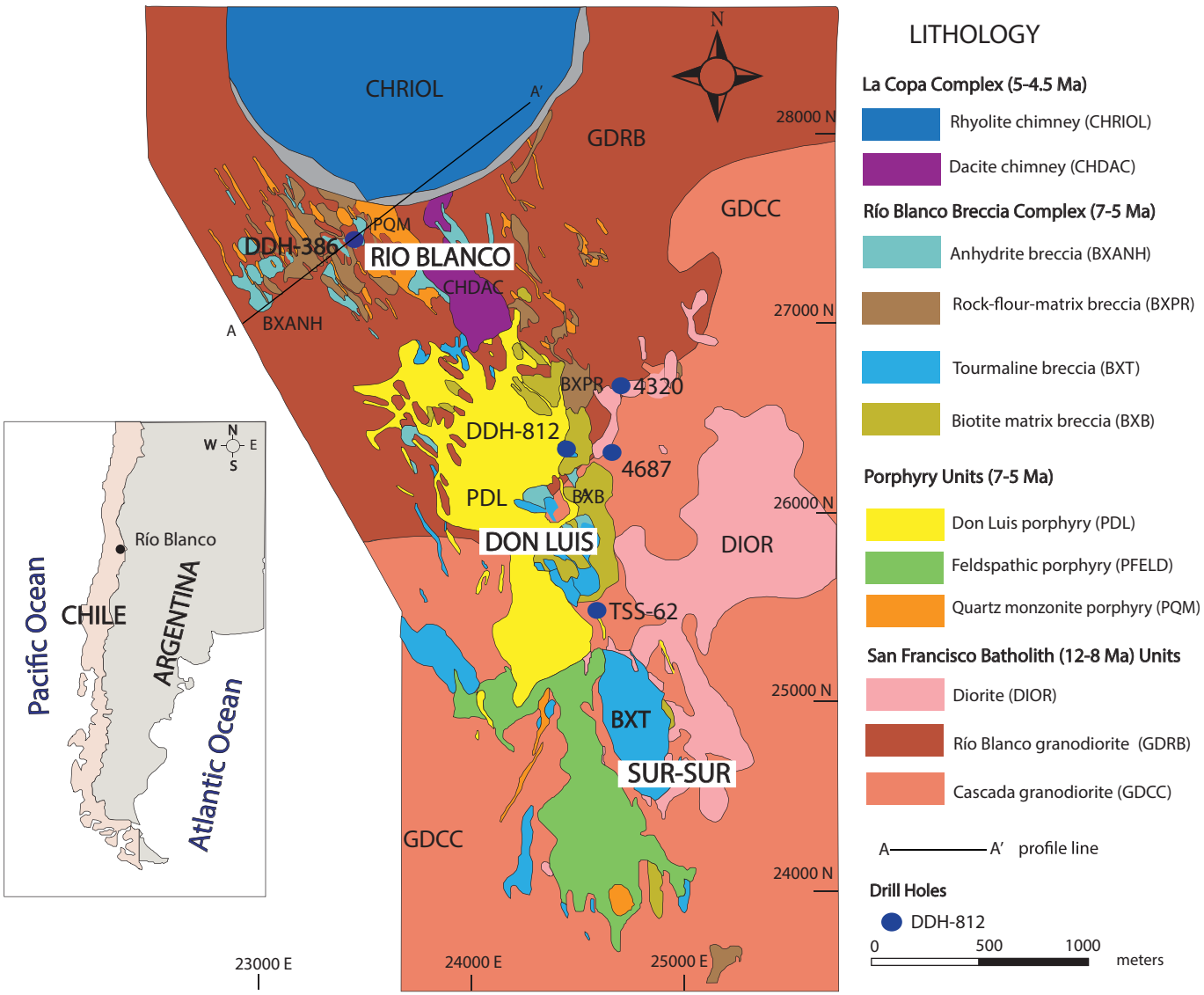

Fig. 1. Geology of the Río Blanco porphyry Cu-Mo deposit. Modified after G. Ferraz and J. Cruz (unpub. report, 2011) and Crespo et al. (2018). Inset shows location of Rio Blanco within Chile.

the diorite (8.19 ± 0.16 Ma) (Fig. 1)—and for late mineralized and barren porphyries and diatremes that intruded the San Francisco batholith and the Farellones Formation (Fig. 2A). These latter units are the quartz monzonite porphyry (6.32 ± 0.09 Ma), the feldspar porphyry (5.84 ± 0.09 Ma), the Don Luis porphyry (5.23 ± 0.07 Ma), and the dacitic chimney (4.92 ± 0.1 Ma).

Several breccia events are recognized in Río Blanco including (1) igneous, (2) igneous/hydrothermal, (3) hydrothermal (biotite- and tourmaline-bearing), and (4) rock-flour breccias (Frikken et al., 2005; Toro et al., 2012). The magmatic, magmatic-hydrothermal breccia complex, and tourmaline breccias are closely related to the porphyry units, and the bulk of the Cu sulfide mineralization occurs as cement in these breccias (Frikken, 2004). Magmatism at the Río Blanco porphyry deposit ended with the emplacement of the La Copa Volcanic Complex, which is located in the northern part of the deposit (Fig. 1) and comprises crystalline tuffs (dacitic chimney; U-Pb zircon age of 4.92 ± 0.1 Ma) and lithic tuffs (Rhyolitic chimney; U-Pb zircon age range 4.92 ± 0.09–4.69 ± 0.23 Ma) (Deckart et al., 2005, 2013; Toro et al., 2012).

Hydrothermal alteration and mineralization

The hydrothermal alteration at the Río Blanco porphyry is characterized by a deep, early potassic event associated with the porphyry intrusive phases (Fig. 2B; Table 1). It is represented by abundant secondary biotite, K-feldspar, minor albite, and anhydrite (G. Ferraz and J. Cruz, unpub. report, 2011), with associated chalcopyrite with lesser bornite, molybdenite, and minor pyrite. Coeval with the development of the potassic alteration, in the most external portions of the system, the alteration is dominated by a chlorite-epidote (propylitic) assemblage (Fig. 2B) with albite, magnetite, rutile, and local actinolite-tremolite as accessory phases. Sulfides in the chlorite-epidote zone include mainly disseminated pyrite. The phyllic stage is superimposed on the potassic alteration and is characterized by gray-green sericite that varies from strong to weak from the center to the outer zones of the deposit (Fig. 2B). In the upper section of the deposit (e.g., 3,400–3,600 m a.s.l.), a late-stage quartz-sericite alteration event is also recognized with quartz, sericite, pyrite, minor chalcopyrite, and Cu sulfosalts.

The potassic alteration is accompanied by four types of veinlets (G. Ferraz and J. Cruz, unpub. report, 2011) (Fig. 3A-D):

1. Early biotite veins correspond to irregular, fine biotite ± quartz ± chalcopyrite-bornite veinlets with or without a biotite halo, usually not exceeding 10-mm width.
2. Early biotite transitional veins, also known as background potassic alteration, have granular texture with quartz, K-feldspar, anhydrite, and sulfides with biotite halos. The early biotite transitional are thicker than early biotite veinlets (commonly >10 mm width), and chalcopyrite and bornite can be present in these veinlets or in the halo.
3. A-type veinlets are sinuous and discontinuous with a granular texture composed of quartz ± K-feldspar ± anhydrite ± chalcopyrite. They have narrow halos of K-feldspar and/or albite. In some veinlets, molybdenite mineralization occurs together with chalcopyrite.

Table 1. Description of the Alteration Types in the Río Blanco Deposit Porphyry Cu-Mo Deposit, Central Chile

Alteration types		Preserved texture	Vein type	Description	Associated mineralization	Total sulfides	Associated alteration
Potassic	FBt	≥85–90%	<5% type EB ± EBT ± A ± B ± <5–10% type D ± <15% type C	Disseminated mineralization in the site of biotitized mafic minerals, primary morphology and cleavage of mafic minerals is lost, chalcopyrite is dominant	Chalcopyrite >> pyrite ± bornite, molybdenite; disseminated > veins	≤1.0 –1.5%	Secondary biotite ± secondary magnetite, rutile
	FBt-Cl	≥85–90%	<5% type EB ± <5–10% type C-D	Partial biotitization, biotitized amphibole pseudomorphs, mineralization in biotite guides or sulfide guides, sparse disseminated mineralization	Chalcopyrite, pyrite; disseminated > veins	≤1.0 –1.5%	Secondary biotite ± secondary magnetite, rutile
	Fk-Bt/ Bt-Fk	≥60%	>15–20% type EB ± EBT ± A ± B ± <5–10% type D ± <15% type C	Texture strongly obliterated by potassic alteration with biotitic domains or feldspathic domains, commonly feldspar that is altered to sericite-biotite, disseminated mineralization with recrystallized breccia matrix or EBT veinlets	Chalcopyrite > bornite > pyrite; disseminated > veins (Fk < Bt); veins > disseminated (Bt > Fk)	>1–2%	K-feldspar ± secondary biotite ± sericite ± tourmaline
Propylitic	FCl-Ep	≥80–90%	<20% type C-D ± <5% type EB	Mafic minerals retain primary morphologies and cleavage, broad chloritization and accessory epidote; scarce disseminated mineralization	Pyrite > chalcopyrite; veins >> disseminated	≤1.0%	Chlorite, epidote ± albite, rutile, and occasionally actinolite-tremolite
Gray-green sericite	GGS	≥60%	>10% type C <5–15% type D	Host rock is strongly obliterated by gray-green sericite alteration associated with veinlets, halos of breccias, abundant disseminated mineralizations, and/or halos of veinlets	Chalcopyrite > pyrite ± bornite	>1–2%	Sericite ± quartz ± secondary biotite
Quartz-sericite	QS	≥60%	>20% type D-E	Texture is obliterated by quartz-sericite with presence of white clays, local development of chlorite, and common presence of disseminated carbonates	Pyrite > chalcopyrite >> enargite-tennantite-tetrahedrite >> sphalerite; veins >> disseminated	≥3–4%	Sericite ± quartz ± carbonates, clays, and chlorite

Abbreviations: Bt > Fk = biotite > K-feldspar, EB = early biotite, EBT = early biotite transitional, FBt = background biotite, FBt-Cl = background biotite-chlorite, FCl-Ep = background chlorite-epidote, Fk > Bt = K-feldspar > biotite, GGS = gray-green sericite, QS = quartz-sericite

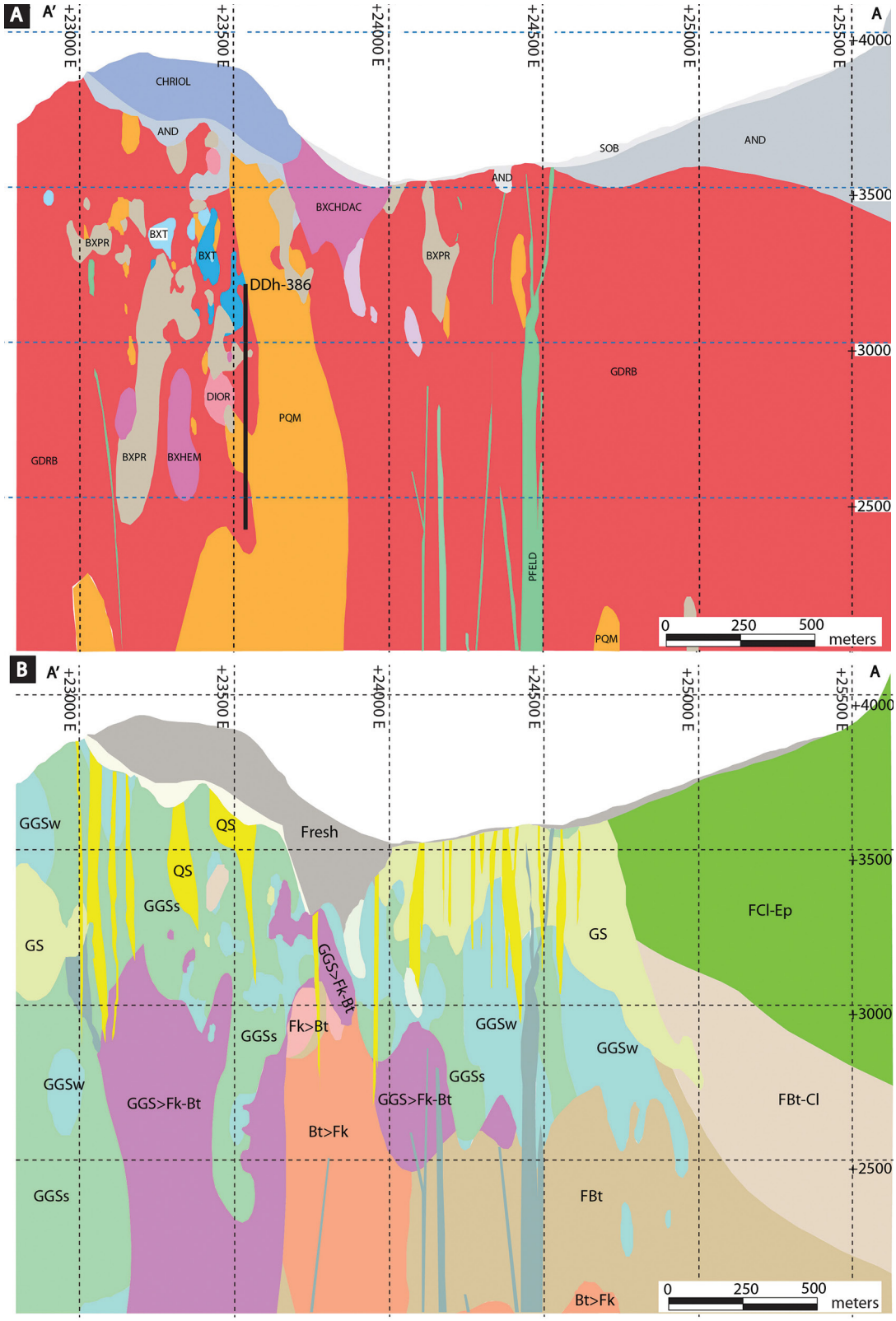

Fig. 2. A) Representative cross section for the Río Blanco deposit. Drill hole DDH-386 is shown in black. The legend of the lithology is presented in Figure 1. B) Cross section A'-A showing the distribution of alteration zones in the Río Blanco sector. Abbreviations: AND = andesite, Bt > Fk = biotite > K-feldspar, BSCHDAC = dacite chimney breccia, BXHEM = hematite breccia, BXT = tourmaline breccia, FBt-Cl = background biotite-chlorite, FCl-Ep = chlorite-epidote, Fk > Bt = K-feldspar > biotite, GGS > Fk-Bt = gray-green sericite > K-feldspar-biotite, GGSm = moderate gray-green sericite, GGSs = gray-green sericite strong, GGSw = weak gray-green sericite, GS = gray sericite, QS = quartz-sericite, SG = gray sericite, SOB = overburden.

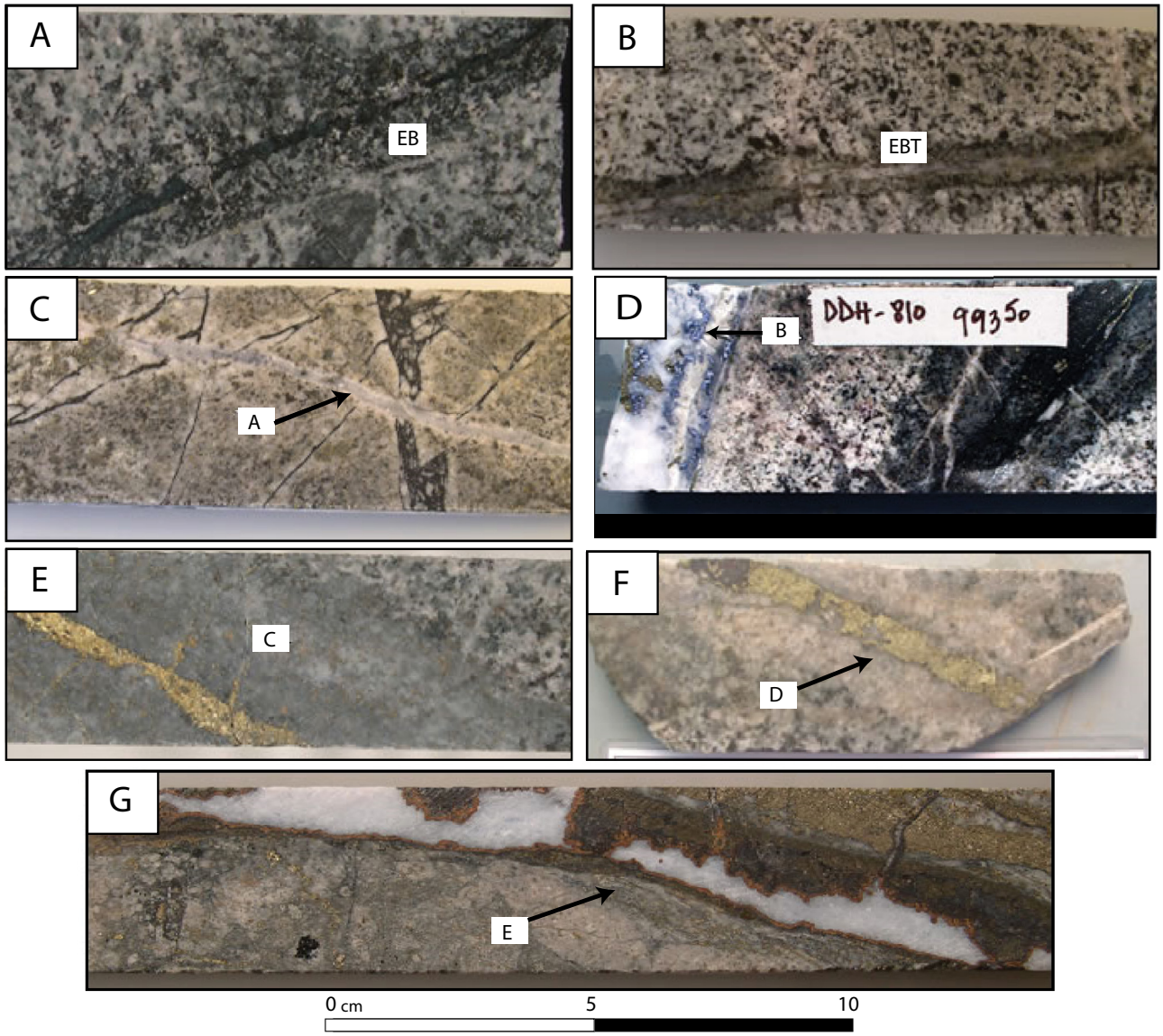

Fig. 3. Photographs of main vein types at Río Blanco. A) Early biotite (EB)-type vein with green micas and biotitic alteration halo. B) Early biotite transitional (EBT)-type vein with biotitic alteration halo. C) A-type vein with quartz and a halo of K-feldspar alteration, crosscutting an early biotite-type vein. D) B-type vein, composed of quartz-molybdenite-chalcopyrite and a K-feldspar halo. E) C-type vein with gray-green sericite-quartz-biotite-chlorite-chalcopyrite-pyrite. F) D-type vein with quartz-chalcopyrite-pyrite and a halo of quartz-sericite-kaolinite. G) E-type vein with quartz-pyrite-chalcopyrite-tennantite-tetrahedrite-enargite-carbonates and a quartz-sericite halo.

4. B-type veinlets are millimeter- to centimeter-thick planar, continuous, and banded, usually without an alteration halo or with millimeter-thick halos of albite-K-feldspar. B-type veinlets show a central quartz suture and are constituted mainly by quartz, typically with anhydrite, molybdenite, chalcopyrite, pyrite, and/or bornite.

The phyllic alteration is defined by the development of C-type veinlets of gray-green sericite comprising phyllosilicate minerals such as green micas (phengite-celadonite) and sericite (Fig. 3E). Sulfide minerals within C-type veinlets are predominantly chalcopyrite ± bornite ± pyrite. The late-stage quartz-sericite alteration event is characterized by the presence of D-type veinlets, which are composed of quartz + pyrite ± chalcopyrite and sericite (illite) + clays (kaolinite-smectite) halos with pyrite > chalcopyrite (Fig. 3F). White mica in D-type veinlets tends to be fine grained in comparison with coarse sericite in C-type veinlets. Late E-type veinlets are composed of quartz + carbonates (siderite-ankerite) + pyrite ± gypsum ± sphalerite ± tennantite ± tetrahedrite ± enargite-luzonite ± galena ± bornite with a white-mica halo (Fig. 3G).

Samples and Methods

Statistical analysis of the ICP-MS database and sulfide sample selection

An ~10,000-sample multielement ICP-MS database was provided by CODELCO-Andina for analysis. The 51-element

whole-rock geochemical database, which also includes geologic drill core mapping attributes, was statistically analyzed to undertake a comprehensive examination of elemental correlations at the deposit scale with emphasis on the Ag grades. First, a correlation matrix analysis of all elements was carried out, highlighting moderate to strong positive correspondences between Ag and associated elements. Secondly, a descriptive statistical analysis was performed to graphically represent the distribution of Ag at the deposit scale using box plots (Fig. 4) considering mining areas, elevation, lithology, and alteration zones. In addition, contour Ag and Cu grade maps were constructed to obtain information about the distribution of these elements (Fig. 5). Statistical analysis was performed by using the ioGAS™ 6.2 software.

Based on the statistical analysis of the ICP-MS database, a total of 28 core samples were selected from drill cores that crosscut all the mineralization and alteration zones at the Río Blanco PCD. The samples were selected based on their Cu and Ag grades (>3 ppm Ag). To ensure representativeness, samples were selected considering the spatial distribution of alteration types and sulfide mineralization. Polished thin (30 μm) and thick (100 μm) sections were prepared for SEM, EMPA, and LA-ICP-MS analyses. Both sulfides (chalcopyrite, bornite, and pyrite) and Cu sulfosalts (enargite, tetrahedrite, and tennantite) were investigated.

SEM

Sulfides and Cu sulfosalts were inspected for the presence of micro- to nanometer-sized inclusions by using a combination of conventional and FE-SEM techniques. The SEM observations were carried out at the Andean Geothermal Center of Excellence (CEGA) in the Department of Geology, Universidad de Chile, using a FEI Quanta 250 SEM equipped with secondary electron (SE), backscattered electron (BSE), and energy dispersive X-ray spectrometry (EDS) detectors. The analyses were carried out with an accelerating voltage of 15 to 20 kV and an emission current of ~80 μA, a takeoff angle ~35°, a 4- to 5-μm beam diameter, and a working distance of ~10 mm. Semiquantitative EDS spot analysis was used to perform a preliminary chemical assessment of mineral phases and inclusions.

High-resolution imaging of micro- to nanosized inclusions within sulfides and sulfosalts was achieved by using FE-SEM. Observations were performed by using a FEI Quanta 250 field emission gun at the Center for Research in Nanotechnology and Advanced Materials (CIEN) at the Pontificia Universidad Católica de Chile, Santiago, Chile. The FE-SEM is equipped with an in-column detector for SE, BSE, and EDS detectors. Analyses were accomplished by using an accelerating voltage of 20 kV, a ~4-μm beam diameter, a takeoff angle ~35° to 37°, a live time of 45 s, and a working distance of ~10 mm.

EMPA

Major and minor element concentrations in pyrite, chalcopyrite, bornite, enargite, tennantite, and tetrahedrite were determined by EMPA using a JEOL JXA-8230 Superprobe at the LAMARX Laboratory of the Universidad Nacional de Córdoba, Argentina. Elements and X-ray lines used for the analysis were Hg (Mα), Te (Lα), Se (Lα), Bi (Mα), Au (Mα), S (Kα), Fe (Kα), Co (Kα), Zn (Kα), As (Kα), Ag (Lα), Pb (Mβ), Sb (Lα), Cu (Kα), Ni (Kα), and Mn (Kα). Operating conditions included an accelerating voltage of 20 kV, a beam current of 20 nA, and a beam diameter of ~1 μm. Counting time was 40 s for Hg, Te, Se, Bi, Au, S, Fe, Co, Zn, As, Ag, Pb, Sb, Cu, Ni, and Mn. Standard specimens used for calibration were HgTe (for Hg and Te), NiSe (for Ni and Se), Bi_2S_3 (for Bi), Au (for Au), $CuFeS_2$ (for Cu, Fe, and S), $CoAs_3$ (for Co), ZnS (for Zn), NiAs (for As), Ag^0 (for Ag), PbS (for Pb), Sb_2S_3 (for Sb), and Mn^0 (for Mn). Wavelength-dispersive spectrometry (WDS) X-ray maps were acquired using the calibration setup described above. Map acquisition was performed using an accelerating voltage of 20 kV, a beam current of 100 nA with 2- × 2-μm pixel dimension, and a counting time of 40 ms/step per pixel.

LA-ICP-MS analyses

Trace element concentrations were determined by LA-ICP-MS on selected grains of pyrite, chalcopyrite, bornite, enargite, tennantite, and tetrahedrite. LA-ICP-MS analyses were carried out at the CEGA Mass Spectrometry Laboratory, Geology Department, Universidad de Chile, using a 193-nm ArF excimer laser (Teledyne-Photon Machines Analyte 193) coupled to a quadrupole ICP-MS (Thermo Fisher Scientific iCAP Q). Prior to each analytical session, the ICP-MS was tuned while ablating a NIST SRM 610 glass to ensure acceptable levels of plasma robustness (i.e., $^{238}U^+/^{232}Th^+$ between 0.95 and 1.05), oxide production ($ThO^+/Th^+ < 0.5\%$), and double-charged production ($^{22}M^+/^{44}Ca^{++} < 0.01\%$). Ablation was carried out using a laser pulse frequency of 4 Hz, energy density of ~1.5 J/cm^2, and a spot size of 40 μm in most cases. Helium was used as carrier gas. Each spot was ablated for 30 s following 30 s of gas background collection. The following isotopes were monitored: ^{34}S, ^{51}V, ^{52}Cr, ^{53}Cr, ^{55}Mn, ^{57}Fe, ^{59}Co, ^{60}Ni, ^{63}Cu, ^{65}Cu, ^{66}Zn, ^{69}Ga, ^{72}Ge, ^{73}Ge, ^{75}As, ^{77}Se, ^{82}Se, ^{95}Mo, ^{97}Mo, ^{105}Pd, ^{107}Ag, ^{109}Ag, ^{111}Cd, ^{115}In, ^{118}Sn, ^{120}Sn, ^{121}Sb, ^{123}Sb, ^{125}Te, ^{182}W, ^{185}Re, ^{189}Os, ^{195}Pt, ^{197}Au, ^{202}Hg, ^{205}Tl, ^{206}Pb, ^{207}Pb, ^{208}Pb, and ^{209}Bi. A dwell time of 10 ms was used for all elements, except for Ag, Cd, In, Sn, Te, Au, and Bi, for which 30 ms was used. The calibration procedure considered both an external and internal standard calibration (Longerich et al., 1996). The MASS-1 pressed synthetic sulfide reference material (Wilson et al., 2002) was used as the primary standard, and the Fe concentration obtained previously by EMPA was used as the internal standard. In addition, the GSE-1G glass reference material (Jochum et al., 2005) was employed as a secondary standard for quality control. External standard measurements were performed at the beginning and at the end of each analytical round of 20 spot analyses. Data integration and reduction was carried out using Iolite v. 2.5 (Paton et al., 2011). LA-ICP-MS maps were obtained by a series of lines of continuous ablations spaced at 10 μm each. The spot size was 10 μm with a laser pulse frequency of 10 Hz and an energy density of ~ 4 J/cm^2. The scanning speed was 10 μm/s. Preablation was performed with a spot size of 30 μm, a repetition rate of 30 Hz, and scanning speed of 30 μm/s to eliminate possible surface contamination. The isotopes selected for the ablation were adjusted to obtain a sweep time of ~2 ms; all the elements had an analysis time of 0.01 ms, with the exception of Zn and Se (0.15 ms).

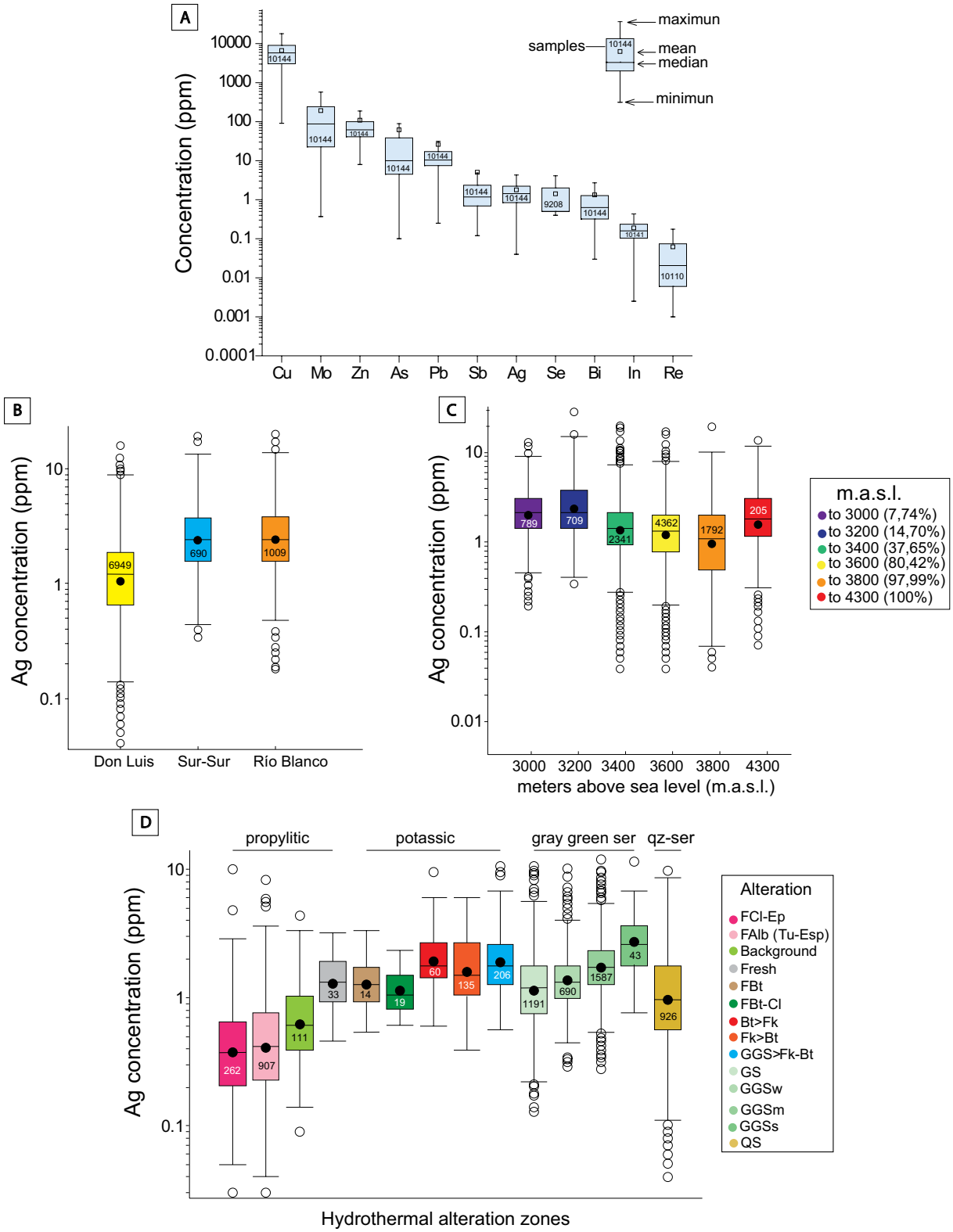

Fig. 4. Statistical analysis of the drill core geochemical data set from Río Blanco. A) Concentration box plot showing Ag and other elements of interest. Data are plotted in parts per million (ppm) on a logarithmic scale. B) Ag concentration box plot according to mining areas in the Río Blanco deposit. C) Ag concentration box plot based on the elevation. D) Ag concentration plotted as a function of the hydrothermal alteration type. Bt > Fk = biotite > K-feldspar, Falb-(Tu-Spec) = albite (tourmaline-specularite), FBt = background biotite, FBt-Cl = background biotite-chlorite, FCl-Ep = background chlorite-epidote, Fk > Bt = K-feldspar > biotite, GGS > Fk-Bt = gray-green sericite > K-feldspar-biotite, GGSm = moderate gray-green sericite, GGSs = strong gray-green sericite, GGSw = weak gray-green sericite, GS = gray sericite, QS = quartz sericite.

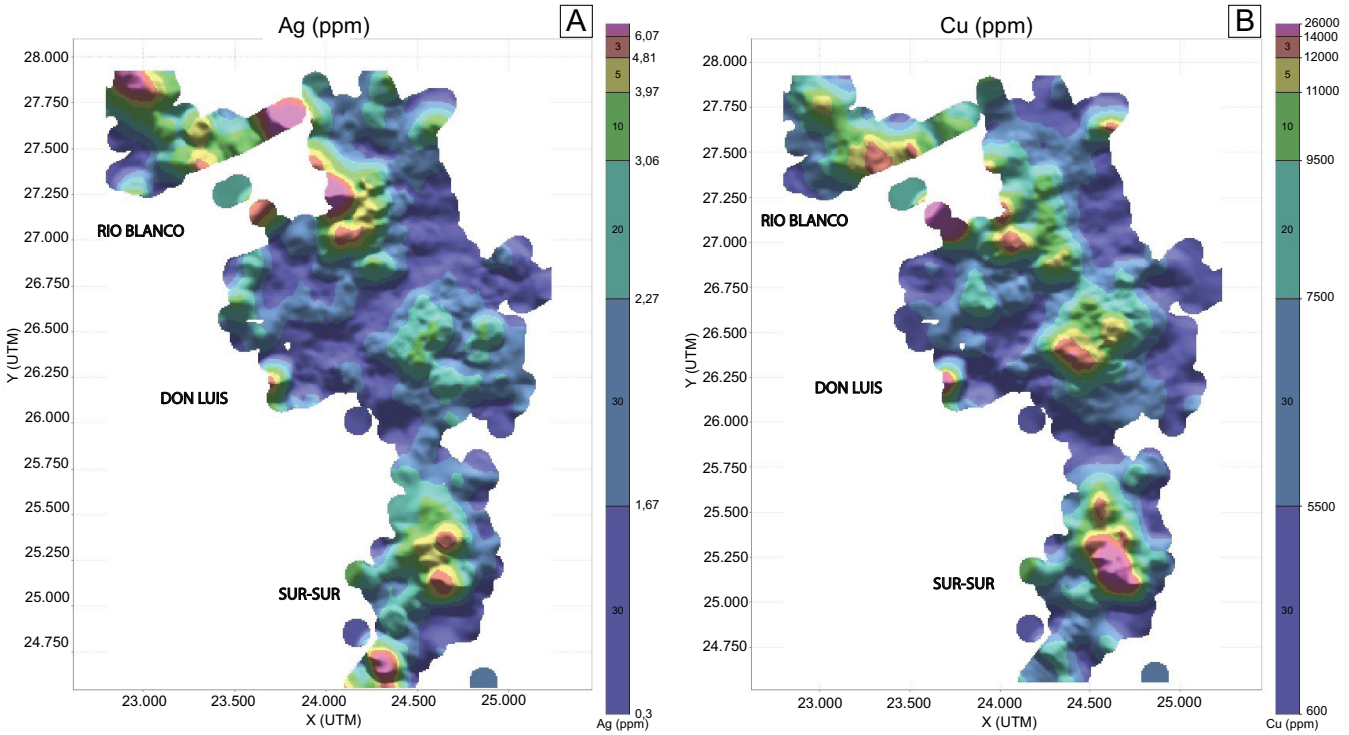

Fig. 5. Plan view contour maps of Ag (A) and Cu (B) grades in the Río Blanco deposit. Warmer colors indicate higher concentrations according to the color bars.

Results

Silver distribution and elemental correlations

Figure 4 shows the concentrations of Ag and associated elements in Río Blanco minerals, illustrated as box plots. The general distribution of Ag and Cu in Río Blanco is illustrated by contour grade maps and show a strong correspondence between both elements (Fig. 5). The highest Cu and Ag grades are found in the three main ore centers: Río Blanco (underground mine) and Don Luis and Sur-Sur (both open pits). All EMPA and LA-ICP-MS analyses are presented in Appendices 1 through 9.

The concentration range of Cu, Mo, and several trace elements, including Zn, As, Pb, Sb, Se, Bi, In, Re, and Ag, are shown in Figure 4A as reference (App. 10). The highest Ag concentration occurs in the Río Blanco mine (0.48–14.12 ppm, median of 2.43 ppm) and Sur-Sur open pit (0.44–13.9 ppm, median of 2.41 ppm), whereas in the Don Luis pit, Ag concentration varies from 0.13 to 8.79 ppm with a median of 1.21 ppm (Fig. 4B). Silver concentrations do not vary significantly with elevation (Fig. 4C). The deepest sample is located at 2,399 m a.s.l. and the shallowest at 4,230 m a.s.l. (elevation variation of ~1,800 m). The highest average values of Ag are located between 2,400 and 3,200 m a.s.l., with an average value of 2.1 ppm, whereas from 3,400 to 3,800 m a.s.l. the average Ag content is 1.2 ppm. From 3,800 to 4,300 m a.s.l. the Ag average grade is 1.8 ppm.

The correlation analysis of the whole-rock ICP-MS data set for 51 elements indicates that Ag shows a strong positive correlation with Cu (r = 0.71) and a moderate positive correlation with In (r = 0.53) and Se (r = 0.51). Silver r values (App. 11) are illustrated in Figure 6 where warm colors in the binary plots represent a higher degree of interactions between element pairs.

Noticeable variations in the Ag concentration are related to the different hydrothermal alteration types (Fig. 4D). The propylitic zone has the lowest average Ag values (0.59 ppm), while the potassic zone presents the highest average Ag concentrations (2.01 ppm). The transitional gray-green sericite zone (phyllic alteration, 1.72 ppm Ag) shows increasing Ag contents as the degree of the alteration increases from gray sericite (least intense) to strong gray-green sericite (most intense). Quartz-sericite alteration has an average Ag content of 1.35 ppm. Overall, the Ag concentration in Cu mineralized rocks at Río Blanco ranges between 0.04 and 28.1 ppm with an average value of 1.78 ppm (App. 10).

The clear Cu-Ag-In correlation is also observed in three representative drill cores from the Río Blanco (drill core DDH-386), Don Luis (drill core DDH-812), and Sur-Sur (drill core TSS-62) ore centers. In these holes Cu, Ag, and In concentrations behave similarly as a function of depth (Fig. 7).

Sulfide/sulfosalt microtextures and Ag mineral inclusions

Figure 8 shows polarized reflected-light microscopy images of representative samples selected for microanalysis. Chalcopyrite is the dominant Cu-Fe sulfide and occurs as anhedral to subhedral crystals, with sizes ranging from 15 μm to 4 mm (Fig. 8A-D). Chalcopyrite occurs in the potassic and phyllic alteration zones as disseminations, as cement of hydrothermal breccias (Fig. 8B), in the suture and halo of veinlets, and intergrown, locally with replacement textures, with pyrite, bornite, and tennantite-tetrahedrite. Bornite occurs as anhe-

dral grains with sizes ranging from 25 μm to 0.8 mm mostly in the potassic zone. Bornite occurs in contact with chalcopyrite (Fig. 8C) and also replacing chalcopyrite. Pyrite occurs as subhedral to anhedral crystals 50 μm to 1.5 mm in size and is abundant in the phyllic alteration zone where it occurs mostly disseminated, in the matrix of breccias and in clasts, and as large aggregates in veinlets. Enargite, tennantite, and tetrahedrite occur as anhedral crystals in the veins of the quartz-sericite alteration zone, related to chalcopyrite-pyrite, filling cavities and fractures in pyrite, and also in grain edge texture with chalcopyrite. These Cu sulfosalts are associated with chalcopyrite and pyrite and range from 10 to 400 μm in size (Fig. 8B).

SEM and FE-SEM analyses indicate several Ag-bearing minerals as inclusions or filling spaces (Fig. 8D; App. 12; Table 2). Silver sulfides (Ag_2S, acanthite or argentite) form fine anhedral crystals with sizes ranging from 1 to 50 μm and occur at the contact between chalcopyrite-pyrite or in chalcopyrite (App. 12) or bornite. Silver sulfides are usually more common in the gray-green sericite to quartz-sericite alteration zones, with a greater number of grains (usually larger in size) observed in the quartz-sericite zone. Silver tellurides

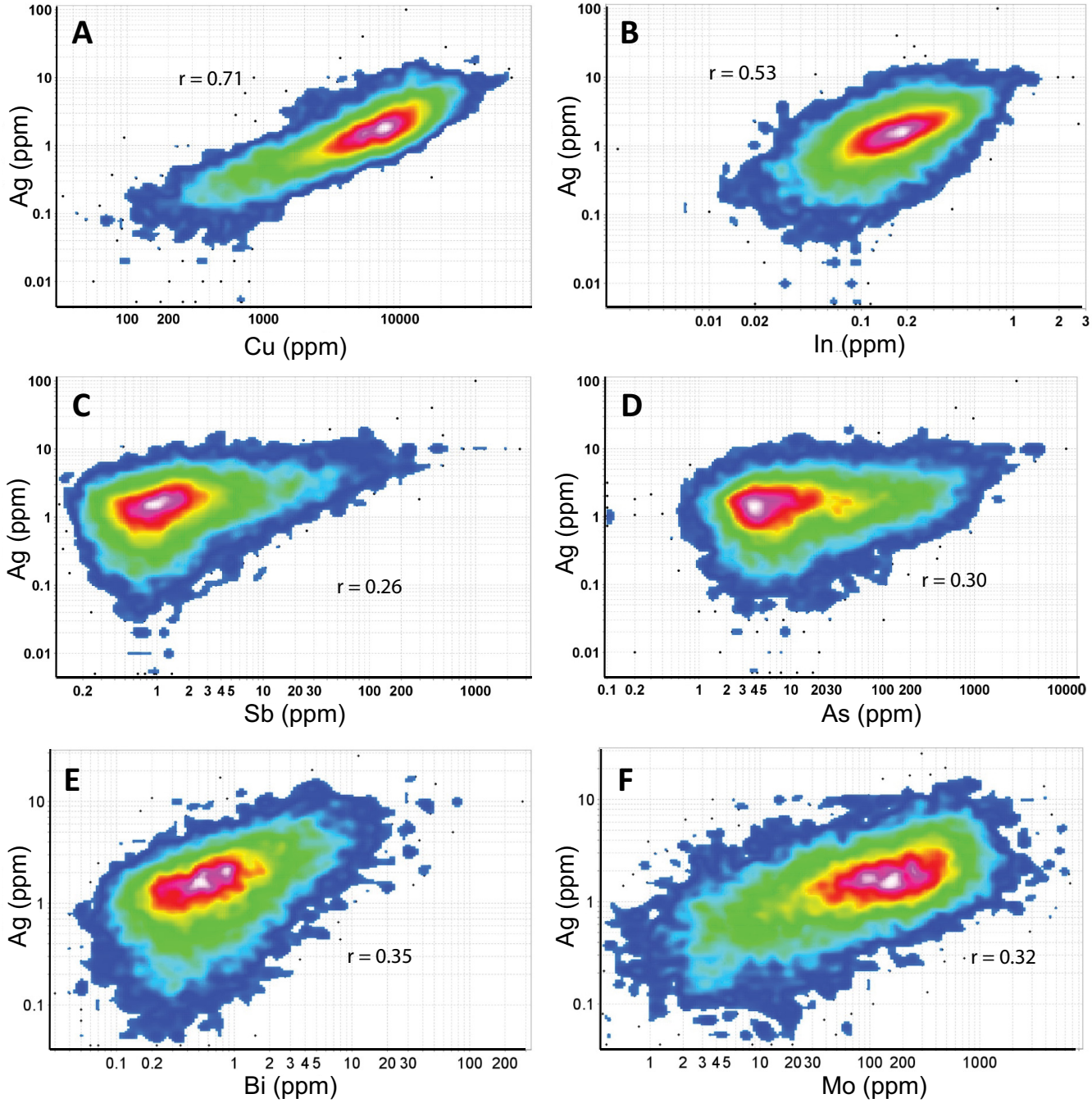

Fig. 6. Binary plots: A) Ag-Cu, B) Ag-In, C) Ag-Sb, D) Ag-As; E) Ag-Bi; and F) Ag-Mo. Data from whole-rock multielement ICP-MS geochemical database of CODELCO-Andina.

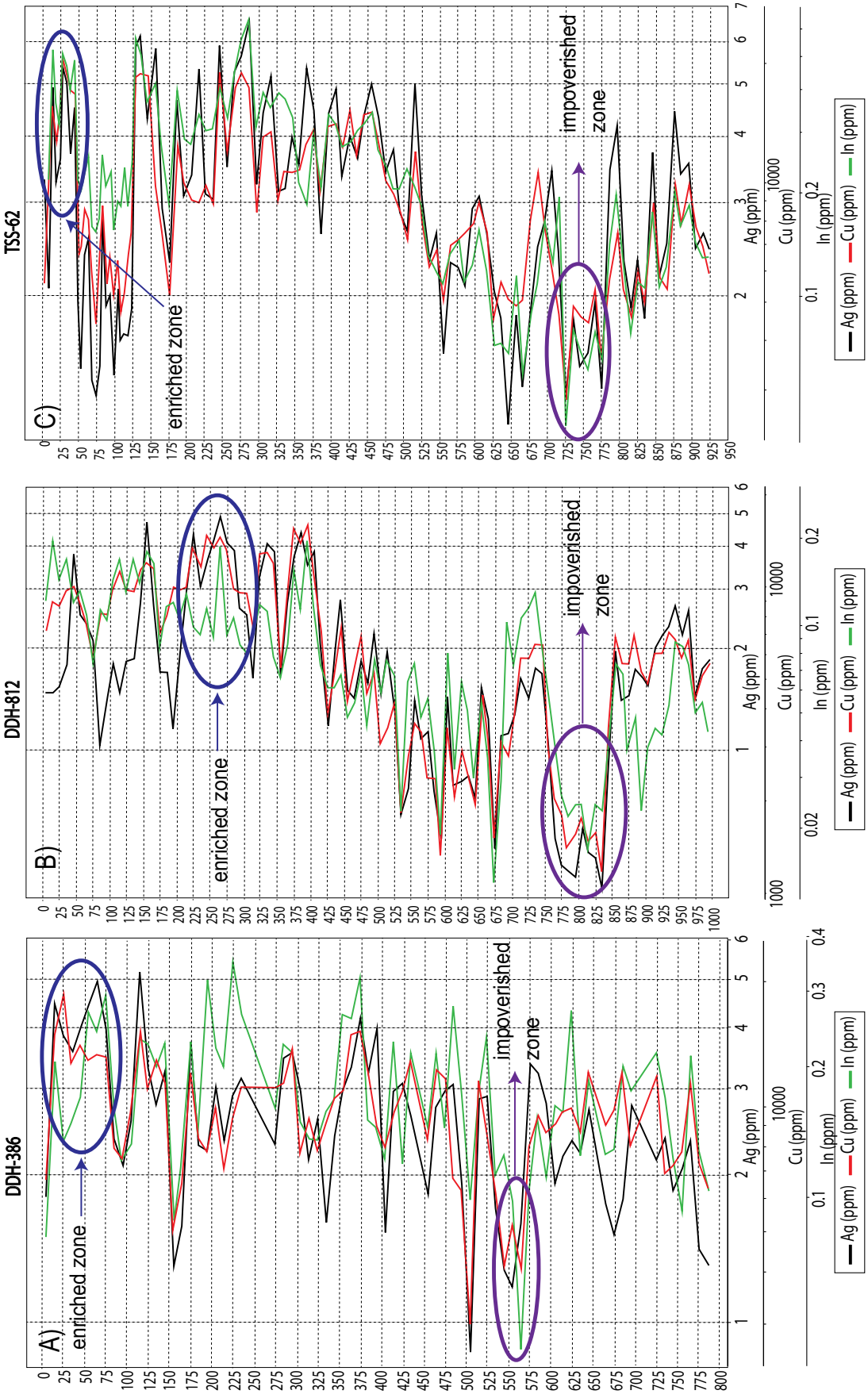

Fig. 7. Drill core profiles showing the concentration (in ppm) of Ag, Cu, and In at depth. Drill hole DDH-386 (A; Río Blanco); DDH-812 (B; Don Luis); TSS-62 (C; Sur-Sur).

such as hessite (Ag_2Te) occur in the potassic alteration zone and to a lesser degree in the gray-green sericite alteration zone. They are typically micro- to nanosized particles (<2 μm) in chalcopyrite and bornite. Some Ag tellurides are associated with Au or Pd, locally forming electrum or merenskyite, $PdTe_2$ (Crespo et al., 2018). In addition, Ag-Cu-As-S and Ag-Bi-Cu-Fe-S assemblages occur locally within the gray-green sericite and quartz-sericite alteration zones, including proustite (Ag_3AsS_3), polybasite ($[Ag,Cu]_6[Sb,As]_2S_7)(Ag_9CuS_4$), and pearceite ($[Ag_9CuS_4])([Ag,Cu]_6[As,Sb]_2S_7$). The minerals are anhedral grains on edges of chalcopyrite or filling cavities or microveinlets in chalcopyrite and pyrite and associated with sulfosalts. Table 2 describes silver mineral occurrences with depth.

Silver contents of sulfides and sulfosalts

EMPA and LA-ICP-MS data are reported in Appendices 1 through 9. Both techniques were used to ensure an optimal combination of spatial resolution and low detection limits (ppm to ppb concentrations). Despite all analyses being performed on clean mineral surfaces, LA-ICP-MS sulfide analyses can be affected by the presence of submicron-sized inclusions containing various elements (see Román et al., 2019, for discussion). Therefore, all LA-ICP-MS spectra were inspected for the presence of spikes indicating mineral inclusions. As a result, the LA-ICP-MS data set for each sulfide and sulfosalt were filtered and represented graphically in box plots as inclusion-bearing and inclusion-free boxes (Figs. 9–12); element concentrations in the former are commonly two orders of magnitude higher than the latter.

Compositional variations of chalcopyrite, bornite, pyrite, enargite, tennantite, and tetrahedrite from the potassic, gray-green sericite, and quartz-sericite alteration zones are described below. A summary of Ag concentrations for each sulfide and sulfosalt mineral is presented in Appendix 13.

Chalcopyrite: All measured chalcopyrite grains have major element concentrations ranging from 33.10 to 35.35 wt % S, 28.07 to 31.26 wt % Fe, and 33.65 to 35.69 wt % Cu, based on EMPA (App. 2).

The Ag concentration in chalcopyrite ($CuFeS_2$) from LA-ICP-MS analyses varies from 0.26 to 348 ppm with an average value of 16.44 ppm (Fig. 9A). The average Ag concentration in

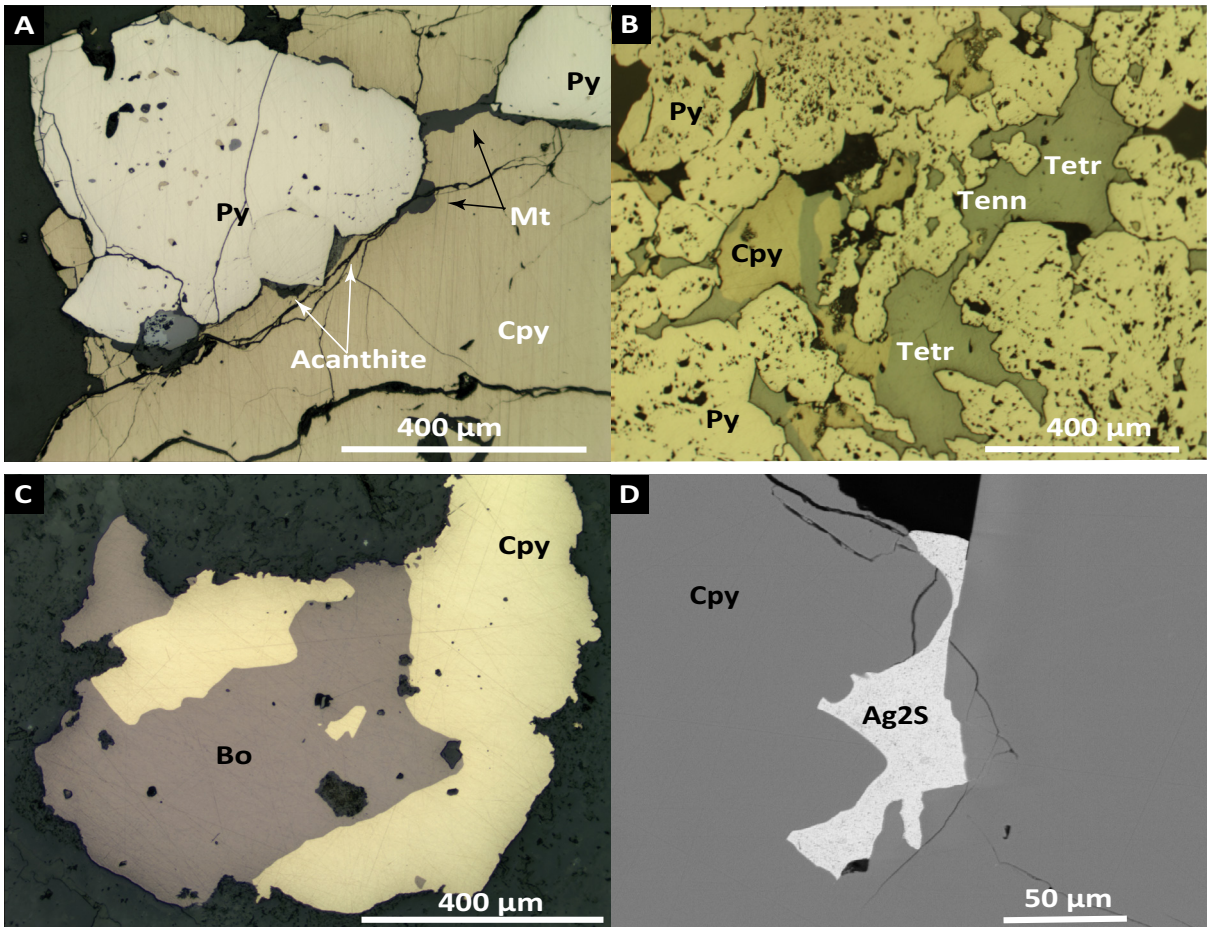

Fig. 8. Reflected-light microscopy photomicrographs and BSE image of sulfide and sulfosalt minerals from representative samples. A) Drill core TSS62, sample 32.4: pyrite and chalcopyrite, with acanthite filling a cavity between chalcopyrite, pyrite, and magnetite (strong gray-green sericite alteration zone). B) Drill core TSS62, sample 286.5: pyrite, chalcopyrite, with replacement of copper sulfosalts (tennantite or tetrahedrite) to chalcopyrite from the quartz-sericite alteration zone. C) Drill core DDH386, sample 618: chalcopyrite intergrown with bornite (moderate gray-green sericite alteration zone). D) Acanthite (Ag_2S) grains in chalcopyrite from the strong gray-green sericite alteration zone (drill core TSS62, sample 129.8). Abbreviations: Bo = bornite, Cpy = chalcopyrite, Mt = magnetite, Py = pyrite, Tenn = tennantite, Tetr = tetrahedrite.

Table 2. Descriptions of Samples Inspected for Silver Minerals Using SEM and FE-SEM Observations

Drill core	Sample name	Meters above sea level (m a.s.l.)	Lithology	Alteration zone	Mineralization	Average Ag (ppm)	Average Cu (ppm)	Ore sulfides and oxides	Silver minerals observed using SEM and FE-SEM
4320	224.2	3,546	Granodiorite	Gray sericite	Py >> Cpy; TS > 1.0	1.13	2,834	Cpy, Py, Mt, Hm, Rt	Ag_2S, AgCuAsFeS, CuAgAsZnFeS, AgCl, AgCuAsS
	373.1	3,420	Granodiorite	Quartz-sericite	Cpy > Py (Sfs); TS > 2.0	4.75	19,900	Cpy, Py, Tn, Gn, Sl, Rt	AgTe, PbAgS, AgCuAsFeS, PbAgTeS, AgCuAsS
	421.1	3,379	Granodiorite	Weak gray-green sericite	Cpy > Py; TS < 2.0	0.91	3,759	Py, Cpy, Mt, Rt	AgTe, AgClBr, AgCu(ClBr)
	531.6	3,286	Granodiorite	Weak gray-green sericite	Cpy > Py; TS < 2.0	1.4	8,838	Cpy, Py, Mt, Rt	AgCuFeAsS
4687	M-3538B	3,247	Granodiorite	Gray-green sericite	Cpy >> Py; TS > 2.0	1.7	7,738	Cpy, Py,	Ag_2S, AgAsS
	M-3535	3,204	Breccia	Gray-green sericite	Cpy > Bo; TS > 1.5	2.42	8,015	Cpy, Py, Bo, Gn, Mo, Mt	AgCuBiFeS
DDH-812	160.93	3,066	Breccia	Potassic	Cpy > Bo; TS > 1.5	2.67	11,498	Cpy, Bo, Mo, Rt,	Ag_2S, AuAg, AgCl
	221.7	3,021	Feldspar porphyry	Potassic	Cpy > Bo; TS > 1.5	4.36	13,460	Cpy, Bo, Mo, Rt	Ag_2S, AgCl
	276	2,984	Breccia	Potassic	Cpy > Bo; TS > 1.5	4.1	13,274	Cpy, Bo, Mo, Gn, Rt	AgTe, AgCl, Ag_2S
	377.5	2,911	Breccia	Potassic	Cpy > Bo; TS > 1.5	3.73	15,478	Cpy, Bo, Mo, Gn, Rt	Ag_2S, AgCl, AgTe, AuAgTe, AuPd
	563.4	2,772	Don Luis porphyry	Potassic	Cpy > Bo; TS < 1.0	1.08	3,360	Cpy, Bo, Gn, Rt	Ag_2S, AgCl, AgClBr
	871	2,548	Diorite	Potassic	Cpy > Bo; TS > 1.5	1.45	5,590	Cpy, Bo, Mo, Rt	Ag_2S, AgCl, AgClBr
DDH-386	133.9	3,050	Tourmaline breccia	Moderate gray-green sericite	Cpy > Py; TS > 2.0	2.78	12,920	Cpy, Bo, Mo, Py, Tn, Mt, Rt	Ag_2S, PbAgS, Pb(AgClSe)S, Ag(SeTe), AuAg, AgTe
	154.2	3,030	Río Blanco granodiorite	Weak gray-green sericite	Cpy > Py; TS < 2.0	1.3	5,060	Cpy, Py, Mo	Ag_2S, PbAgS, Pb(AgCl)S, AgAsS, AgTe, AgPdTe
	459	2,730	Río Blanco granodiorite	Moderate gray-green sericite	Cpy >> Py; TS > 2.0	1.82	8,350	Cpy, Py, Mo, Mt	Ag_2S, PbAgS, AgTe, AgBiS, AgSe, AuAg
	477.9	2,710	Río Blanco granodiorite	Weak gray-green sericite	Cpy > Py; TS < 2.0	2.96	11,700	Cpy, Mo, Rt	Ag_2S, AgTe, AgSbAsS
	564	2,620	Quartz monzonite porphyry	Weak gray-green sericite	Cpy > Py; TS < 2.0	1.59	4,060	Cpy, Bo, Tn, Cc, Rt	Ag_2S, AuAg, Ag(ClBr),
	598	2,590	Río Blanco granodiorite	Potassic with overprinting sericite	Cpy > Bo; TS > 1.5	2.8	8,680	Cpy, Bo, Mo, Rt	Ag_2S, AgTe, AgCl, Ag(ClBr)
	618	2,570	Río Blanco granodiorite	Moderate gray-green sericite	Cpy >> Py; TS > 2	2.18	9,680	Cpy, Bo, Rt, Hm	Ag(SeTe), AuAg, AgCl
	700.1	2,490	Quartz monzonite porphyry	Potassic with overprinting sericite	Cpy > Bo; TS > 1.5	2.77	8,090	Cpy, Bo, Mo, Rt	Ag_2S, AgTe, AgCl, AuAg
TSS-62	32.4	3,630	Tourmaline breccia	Strong gray-green sericite	Cpy >> Py; TS > 2	5.03	18,000	Cpy, Py, Mt, Hm	Ag_2S, AgTe, AgCuS, AgAsS
	129.8	3,543	Tourmaline breccia	Strong gray-green sericite	Cpy > Py; TS < 2	5.87	18,500	Cpy, Py, Mt, Hm, Rt	Ag_2S, AgTe, AuAg, Ag(CuAs)S, AuAg(CuFeAs)S
	286.5	3,400	Tourmaline breccia	Quartz-sericite	Py > Cpy; TS > 2	6.53	17,300	Py, Cpy, Bo, Mo, Tn, Mt, Hm,	Ag_2S, AgBi(CuFe)S, AgBi(CuAs)S
	424.6	3,274	Tourmaline breccia	Potassic	Cpy >> Py; TS > 2	4	15,200	Cpy, Py, Bo, Mt, Hm	Ag_2S, Ag(BiCu)S, AgZnS, AgCl
	693.3	3,033	Cascada granodiorite	Potassic	Cpy > Py; TS > 2	2.76	7,460	Cpy, Py, Tn, Mo, Mt, Rt	Ag_2S, BiCuAgS, AgTe, AgAs, AgCl, Ag(SeTe), Cu(AgAsZn)S
	788	2,953	Quartz monzonite porphyry	Potassic	Cpy > Py; TS > 2	3.45	5,710	Cpy, Py, Tn, Mo, Rt	Ag_2S, AgTe, AgAsS, Pb(AgSe)S, Ag(CuAs)S, Ag(SeTe), Zn(AgFe)S, AgCl

Abbreviations: Bo = bornite, Cpy = chalcopyrite, Gn = galena, Hm = hematite, Mo = molybdenite, Mt = magnetite, Py = pyrite, Rt = rutile, Sfs = sulfosalts, Sl = sphalerite, Tn = tennantite, TS = total sulfides

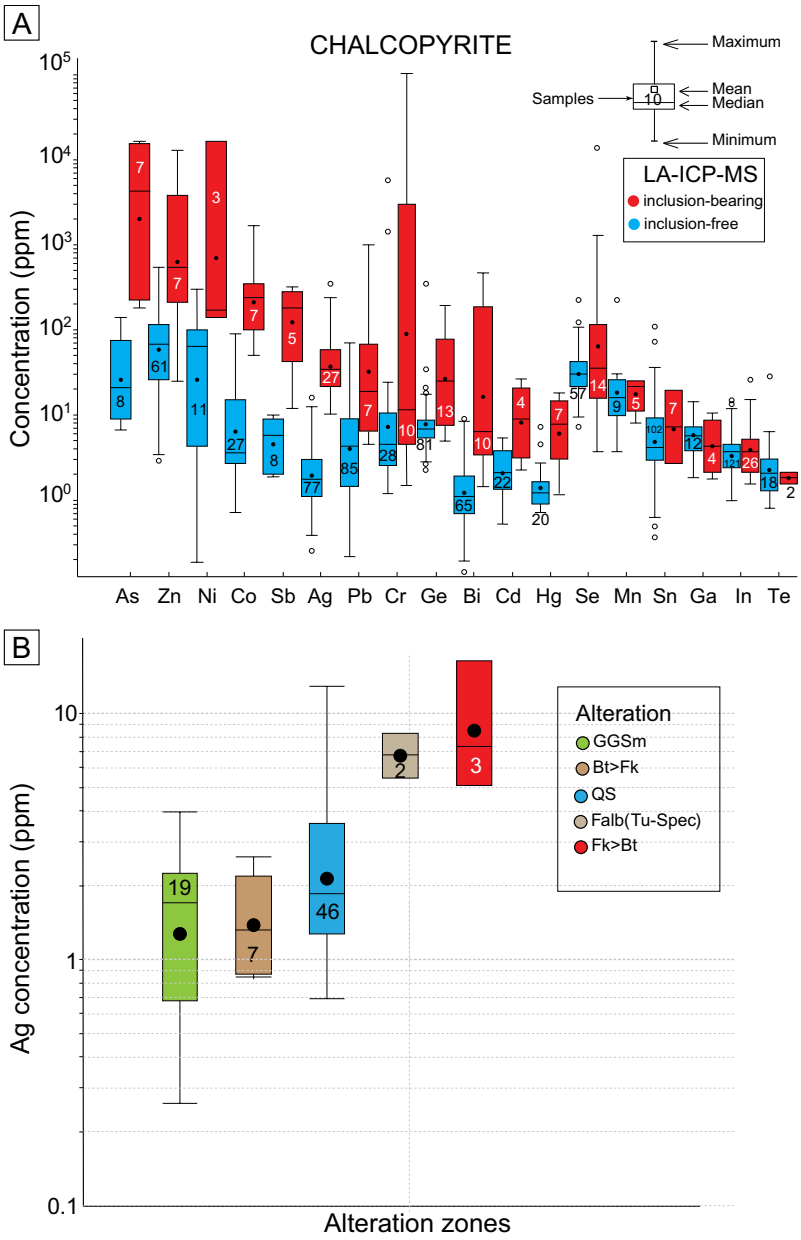

Fig. 9. Box plots of LA-ICP-MS data for selected minor and trace elements in chalcopyrite. Data are plotted in parts per million (ppm) on a logarithmic scale. In each box plot, minimum, median, and maximum concentrations are indicated, and the number of analyses above detection limit for each element is displayed inside each box. A) All data are plotted and separated as inclusion-bearing and inclusion-free analyses (shown in red and blue, respectively). B) Box plot shows the Ag concentration of chalcopyrite from different alteration zones in Río Blanco. Chalcopyrite from the potassic alteration zones (on the left) has a higher Ag content than in the phyllic alteration zones (right). Abbreviations for alteration zones as in Figure 4.

inclusion-free and inclusion-bearing chalcopyrite is 2.75 and 55.4 ppm, respectively (Fig. 9A). Besides Ag, the most abundant trace elements are As (6.8–16,300 ppm), Zn (2.9–13,000 ppm), Ni (0.19–16,000 ppm), Co (0.72–1,700 ppm), Sb (1.9–315 ppm), Cr (1.2–103,000 ppm), Bi (0.14–470 ppm), and Se (3.7–14,100 ppm). These elements (As, Zn, Ni, Co, Sb, Cr, Bi, and Se) are found as inclusions in some chalcopyrite grains by LA-ICP-MS analysis. Indium is present in all LA-ICP-MS analyses (0.55–26.3 ppm, median of 3.68 ppm), with no variations of averages in samples with mineral inclusions. The LA-ICP-MS data varies as a function of alteration (Fig. 9B; "Hydrothermal alteration and mineralization" section). Chalcopyrite from the potassic alteration zone shows the highest Ag concentrations, ranging from 5.1 to 7.3 ppm inclusion free (App. 7). However, chalcopyrite from the less intense potassic alteration zone of biotite has lower Ag values (0.85–2.6 ppm) than Ag concentrations in the moderate gray-green sericite (0.26–3.94 ppm) and quartz-sericite zone (0.69–12.8 ppm) (App. 13). All analyses are in Appendices 2 and 7.

BSE images and WDS X-ray maps of Ag (Lα), As (Lα), and Bi (Mα) of a chalcopyrite-bornite composite grain from the potassic zone (sample DDH812_871) indicate a uniform distribution of Ag in both chalcopyrite and bornite, with the highest concentration in bornite (next section) (App. 14). No mineral inclusions containing Ag or As were identified. Arsenic contents are lower in bornite than in chalcopyrite (App. 14), while Bi is evenly distributed in both sulfides (App. 14). LA-ICP-MS data in this chalcopyrite grain (App. 7, DDH812_871) record values of Ag 1.25 ppm, Pb 0.57 ppm, Se 59 ppm, Ge 7 ppm, In 2.95 ppm, and Sn 8.9 ppm.

Bornite: EMPA and LA-ICP-MS analyses of bornite (Cu_5FeS_4) from the potassic and gray-green sericite zones (Apps. 3, 8) indicate that this sulfide hosts significant trace elements.

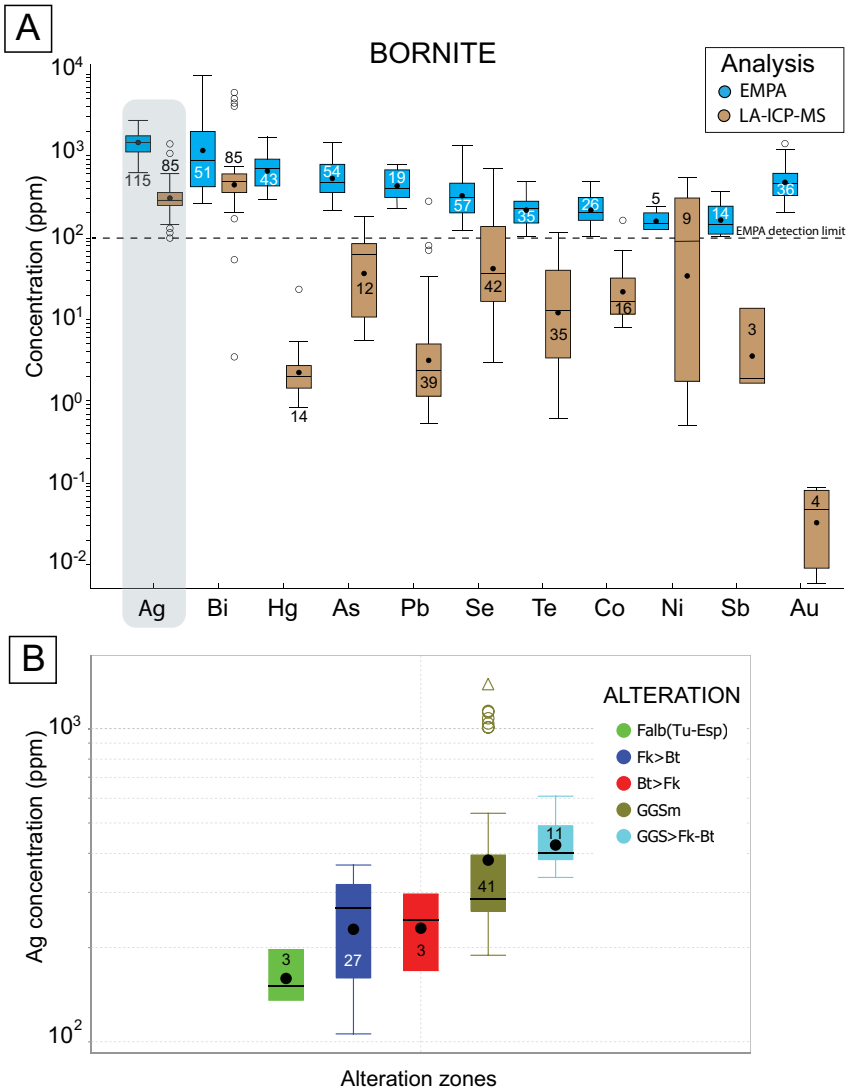

Fig. 10. LA-ICP-MS concentration box plots for selected minor and trace elements in bornite (in ppm and logarithmic scale). In each box plot, minimum, median, and maximum concentrations are marked, and the number of analyses above detection limit for each element is displayed inside each box. A) EMPA and LA-ICP-MS data for bornite are shown in blue and brown, respectively. B) LA-ICP-MS concentrations of Ag in bornite are plotted as a function of alteration types showing higher Ag values in the late stages with respect to the early potassic events. Abbreviations for alteration zones as in Figure 4.

EMPA analysis for the major elements range from 59.45 to 63.9 wt % Cu, 23.93 to 27.44 wt % S, and 10.36 to 12.07 wt % Fe. Most LA-ICP-MS analyses of bornite did not show evidence of mineral inclusions that could affect the data interpretation; hence, all LA-ICP-MS data (Fig. 10) are from inclusion-free bornite, representing the low end of the concentration range (ppm and sub-ppm levels). LA-ICP-MS data from bornite show the highest Ag concentrations in all analyzed sulfides, ranging between 106 and 1,380 ppm, with a median of 285 ppm (avg 356 ppm Ag) (Fig. 10A). Bismuth is also present, between 3.4 and 5,940 ppm with a median of 480 ppm (avg 828 ppm Bi). Other elements detected in minor concentrations are Hg (0.85–23.4 ppm), As (5.6–180 ppm), Pb (0.52–275 ppm), Se (3–700 ppm), Te (0.62–115 ppm), Co (8–160 ppm), Ni (0.51–540 ppm), Sb (1.71–13.6 ppm), and Au (0.01–0.09 ppm) (Fig. 10). LA-ICP-MS data of bornite plotted as a function of alteration (Fig. 10B; "Hydrothermal alteration and mineralization" section for references) indicate that the gray-green sericite moderate zone (463 ppm Ag) and transitional gray-green sericite zone (gray-green sericite > K-feldspar > biotite, 431 ppm) has higher average Ag contents than bornite from the potassic zone (biotite > K-feldspar, 236 ppm; K-feldspar > biotite, 244 ppm). The lowest average values correspond to the background potassic alteration zone (background albite [tourmaline-specularite]) (161 ppm Ag).

LA-ICP-MS trace element maps of a selected bornite grain from the potassic zone (K-feldspar > biotite) (Apps. 8, 15; sample DDH812_377.5) indicate that major elements such as Cu and S have a uniform distribution, except Fe (App. 15), whose concentration is lower at the grain edges. Silver is relatively homogeneous within the grain, although it displays a significantly higher concentration of Ag at the grain rims; this enrichment in Ag at the grain edges correlates spatially with lower Fe concentrations. In addition, some discrete high-count spots suggest the presence of Ag-bearing inclusions. Bismuth and Se show a uniform distribution, whereas Au, Pd, and to a lesser extent Te, Sn, and Pb are heterogeneously distributed in bornite, suggesting the presence of inclusions (App. 15).

Pyrite: Pyrite contains 39.44 to 48.29 wt % Fe, with sulfur contents ranging from 42.88 to 53.55 wt % (EMPA analyses; App. 1).

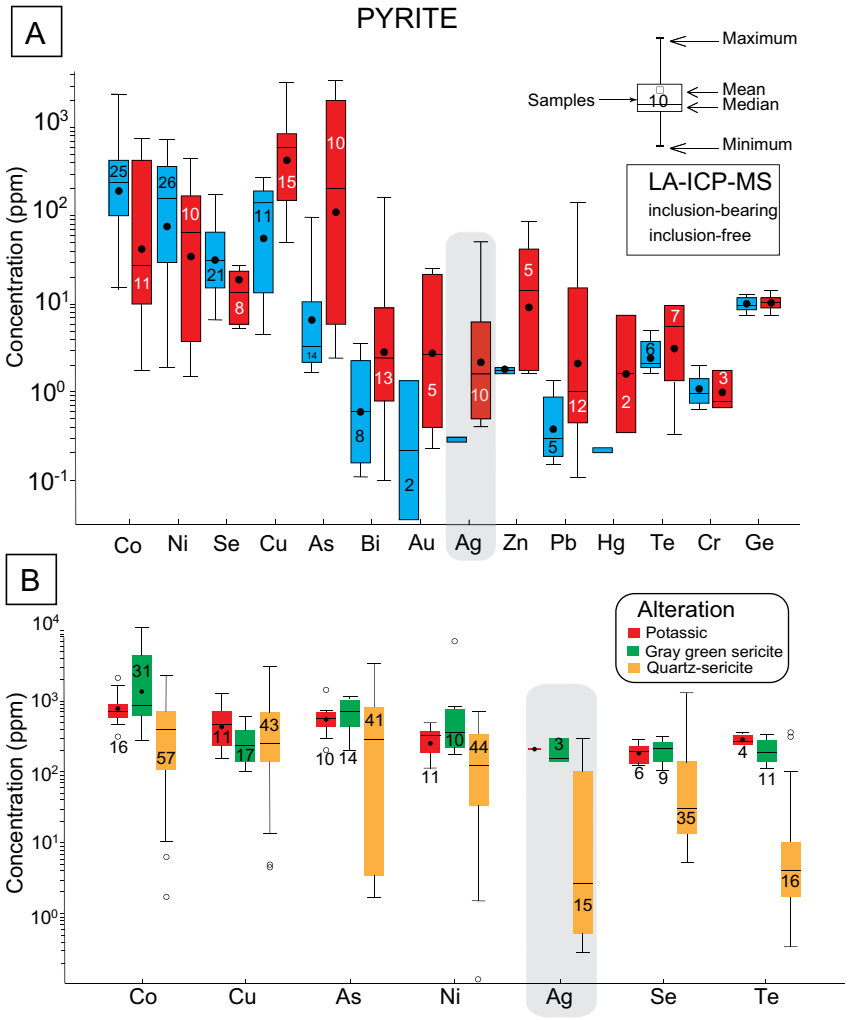

Fig. 11. Box plots showing concentration data for selected minor and trace elements in pyrite. Data are plotted in parts per million (ppm) on a logarithmic scale. In each box plot, minimum, median, and maximum concentrations are marked, and the number of analyses above detection limit for each element is displayed inside each box. A) Inclusion-bearing and inclusion-free analyses are shown as red and blue box plots, respectively. B) Box plot of major and trace elements concentrations in pyrite (EMPA and LA-ICP-MS data) as a function of alteration types.

LA-ICP-MS data of pyrite (Fig. 11A; App. 6) indicate that Ag concentrations are the lowest among sulfides, ranging from 0.29 to 52 ppm with a median content of 0.95 ppm (avg 8.2 ppm). Arsenic and Cu concentrations are high, up to 3,360 and 3,170 ppm, respectively; Co and Ni show concentrations of up to 2,360 and 717 ppm, respectively, and Au ranges from 0.04 to 25.4 ppm (median of 1.31 ppm). Selenium concentrations can attain 1,320 ppm. Other trace elements are mostly below 100 to 200 ppm, i.e., Bi (≤158 ppm), Pb (≤139 ppm), Zn (≤84 ppm), Sb (≤28.7 ppm), In (≤14 ppm), Ge (≤14 ppm), Te (≤10 ppm), Hg (≤7.3 ppm), and Cr (≤1.99 ppm).

The trace element signature of pyrites from different alteration assemblages ("Hydrothermal alteration and mineralization" section; Fig. 11B) is largely from the gray-green sericite and the quartz-sericite alteration zones; pyrite in the potassic zone is scarce. There are no significant variations in trace element concentrations between alteration zones (Fig. 11B), although a few differences stand out. Cobalt, Ni, and Te tend to be more concentrated in pyrite from the earlier stages (gray-green sericite), whereas Se, Cu, As, and Ag are higher in late-stage pyrite from the quartz-sericite zone.

BSE images and WDS X-ray maps for pyrite from the quartz-sericite zone (Fig. 13; sample TSS-62_286.5) indicate that grains are anhedral and have a distinct overgrowth of colloform-like As-Ag-Cu–rich bands (Fig. 13A-D). EMPA spot analyses in the As-Ag-Cu–rich bands show high trace element concentrations—i.e., Ag ~0.59 wt %, As ~11.31 wt %, Cu ~2.76 wt %, Pb ~0.83 wt %, Sb ~0.29 wt %, and Hg ~0.07 wt %—while Fe and S are diminished with respect to the core (~39.49 wt % Fe and ~43.01 wt % S) (App. 1, TSS-62_286.5). Figure 14 shows LA-ICP-MS trace element maps of a selected pyrite grain from the gray-green sericite zone (sample DDH-386_459). Unlike pyrite from the late quartz-sericite zone, pyrite from the former is mostly euhedral and Ag poor and shows a zonation pattern with a Co-Ni-Pb-Bi–rich band in the core (Fig. 14E-H) surrounded by an As-rich band (Fig. 14B). Gold forms micrometric to nanometric inclusions within the As-rich bands (Fig. 14C), and some Ag-bearing inclusions are observed within the pyrite grain (Fig. 14D), although unrelated to the gold inclusions.

Enargite, tennantite, and tetrahedrite: Copper sulfosalts at Río Blanco are found in the quartz-sericite zone in D-type veinlets. EMPA and LA-ICP-MS data of enargite (Cu_3AsS_4), tennantite ($Cu_6[Cu_4(Fe,Zn)_2]As_4S_{13}$), and tetrahedrite ($Cu_6[Cu_4(Fe,Zn)_2]Sb_4S_{13}$) (Apps. 4, 9) indicate Ag, Bi, Cd, Hg, Pb, and In were detected in all Cu sulfosalt analyses. LA-ICP-MS data (Fig. 12) show that the average contents of Ag, Sb, Bi, Cd, Hg, and Co are higher in tetrahedrite than

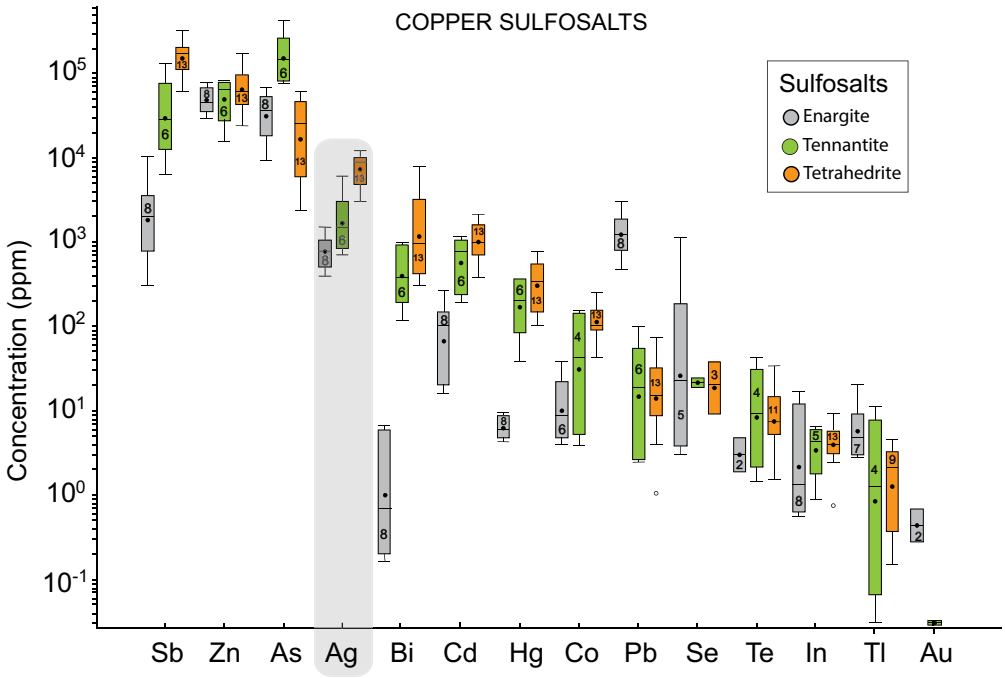

Fig. 12. Box plot showing LA-ICP-MS data for the Cu sulfosalts enargite, tennantite, and tetrahedrite. Data are plotted in parts per million (ppm) on a logarithmic scale. In each box plot, minimum, median, and maximum concentrations are marked, and the number of analyses above detection limit for each element is displayed inside each box.

in tennantite and enargite. Silver is highly concentrated in the copper sulfosalts, ranging from 3,070 to 11,980 ppm in tetrahedrite (avg 7,907 ppm), between 695 and 5,980 ppm in tennantite (avg 2,148 ppm), and from 398 to 1,500 ppm in enargite (avg 820 ppm) (Fig. 12). Bismuth is concentrated in tennantite (up to 1,020 ppm) and tetrahedrite (up to 7,960 ppm) in contrast to enargite (≤6.5 ppm). Indium is homogeneously concentrated within the three Cu sulfosalts, however, at low concentrations, i.e., enargite ≤16.3 ppm, tetrahedrite ≤9.0 ppm, and tennantite ≤6.5 ppm. Gold was only detected in enargite with ≤0.66 ppm.

WDS X-ray maps for selected elements (Ag Lα; Sb Lα; As Kα) in tennantite and tetrahedrite from the quartz-sericite zone (sample TSS62_286.5; Fig. 15) indicate that higher Ag concentrations are associated with higher Sb and lower As contents (Fig. 15 B-D). Thus, Ag is more compatible with tetrahedrite than tennantite.

Discussion

Silver incorporation into sulfides and sulfosalts

The statistical analysis of the ICP-MS database from Río Blanco shows that Ag is primarily concentrated in the Cu-Mo ore zones. This agrees with previous reviews, which concluded that Ag and associated trace elements are generally concentrated in the cores of porphyry Cu deposits (Singer et al., 2008; John and Taylor, 2016). Variations in the Ag concentration in Río Blanco are related to the different hydrothermal alteration types (Fig. 4D). Silver concentrations are lowest in the outer propylitic alteration zone (avg 0.59 ppm) and increase toward the potassic core where concentrations are the highest (avg 2.01 ppm). Silver concentrations in the gray-green sericite zone are also high (avg 1.72 ppm) with increasing Ag contents coupled to degree of alteration.

The overall positive correlation between Cu, Ag, Sb, As, In, Bi, and Mo at the deposit scale (Fig. 6; App. 11) indicates that Ag is associated with sulfide minerals (chalcopyrite, bornite, and pyrite) as well as with Cu sulfosalts (tennantite, tetrahedrite, and enargite). These results are consistent with previous studies, which found that trace metals and metalloids are usually present in solid solution in the Cu-Fe sulfides and sulfosalts in PCDs (Ballantyne et al., 1998; Arif and Baker, 2004; Singer et al., 2008; John and Taylor 2016). The different r values obtained for the element pairs (Fig. 6) are interpreted as a result of sulfide and sulfosalt mineral occurrence and abundance. For instance, the strong correlation observed for Cu-Ag (r = 0.71; Fig. 6A) and Cu-In (r = 0.53; Fig. 6B) in comparison to the low correlation between Ag-Sb (r = 0.26; Fig. 6C) and Ag-As (r = 0.30; Fig. 6D) is most likely due to the different alteration and mineralization events in the deposit, with a lack of As-Sb bearing sulfosalts in the potassic zone.

Chalcopyrite is the most abundant ore sulfide at Río Blanco and contains Ag concentrations that range from sub-parts per million levels to hundreds of parts per million (Fig. 9A; Apps. 2, 7, 10). The highest concentrations of Ag in chalcopyrite are hosted by potassic alteration, which formed at the highest temperature (Fig. 9B). Silver appears to be incorporated mostly in solid solution within the chalcopyrite structure, since Ag follows a behavior similar to that of Cu in the time-resolved downhole profiles collected by LA-ICP-MS (App. 16). Previous studies have shown that chalcopyrite hosts significant amounts of Ag in massive sulfide (Harris et al., 1984; Butler and Nesbitt, 1999) and porphyry-like (Reich et al., 2013b) deposits. On the other hand, elements such as In and Bi can be

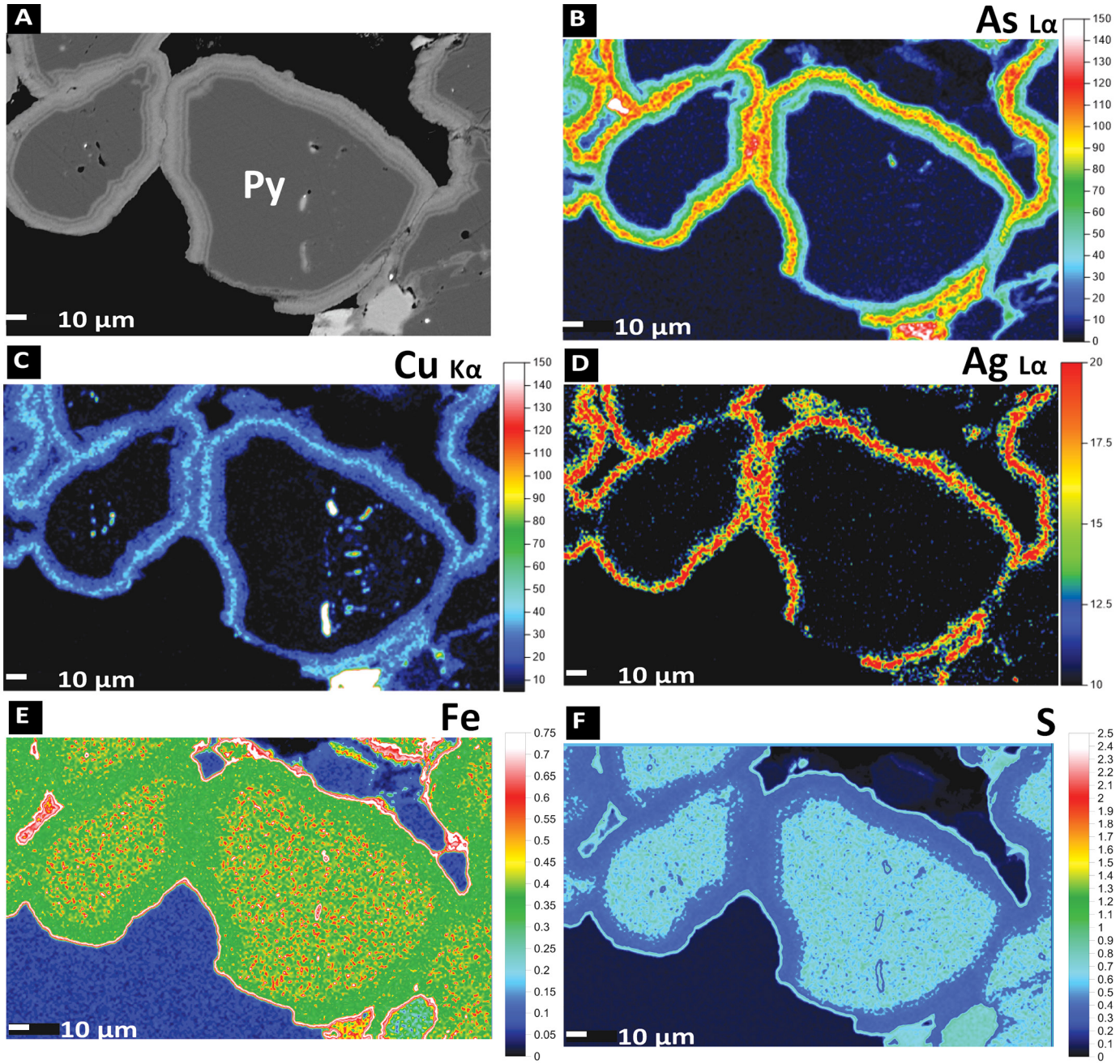

Fig. 13. BSE image and qualitative WDS X-ray maps for pyrite grains from the quartz-sericite alteration zone (drill core TSS-62-sample 286.5). A) BSE image of pyrite (Py) with a distinct compositional oscillatory zoning in the grain edge. B) As (Lα) map. C) Cu (Kα) map. D) Ag (Lα) map. E) Fe (Kα) map. F) EDS S (Kα) map. The WDS maps show distinct oscillatory zonation of As (Lα), Cu (Kα), and Ag (Lα). A color scale bar, which represents the intensity of the detector signal, is shown for each WDS map. Abbreviations: Cpy = chalcopyrite, Py = pyrite, Tenn = tennantite, Tetr = tetrahedrite.

also concentrated in chalcopyrite from various deposit types (Kieft and Damman, 1990; Gena et al., 2013; George et al., 2016, 2018). These elements are also present in chalcopyrite at Río Blanco and correlate positively with Ag at the deposit scale. Therefore, it is likely that Ag replaces monovalent Cu in chalcopyrite (Wei Goh et al., 2006) in a coupled substitution with either In or Bi of the type $Cu_{1-x}Ag_xFe_{1-y}(In, Bi)_yS_2$. In addition, some Ag in chalcopyrite at Río Blanco is contained as discrete Ag mineral inclusions (e.g., Ag_2S or Ag_2Te; Fig. 8; App. 12). This is also interpreted based on the relative difference between the inclusion-free and inclusion-bearing LA-ICP-MS Ag data, i.e., inclusion-bearing data points show higher Ag contents (Fig. 9A). Hence, the highest Ag contents detected in chalcopyrite are most likely related to the presence of submicron-sized Ag-bearing inclusions.

Bornite is less abundant as an ore mineral than chalcopyrite at Río Blanco but is a major host of Ag, as it contains the highest Ag concentration of all analyzed sulfides, ranging from

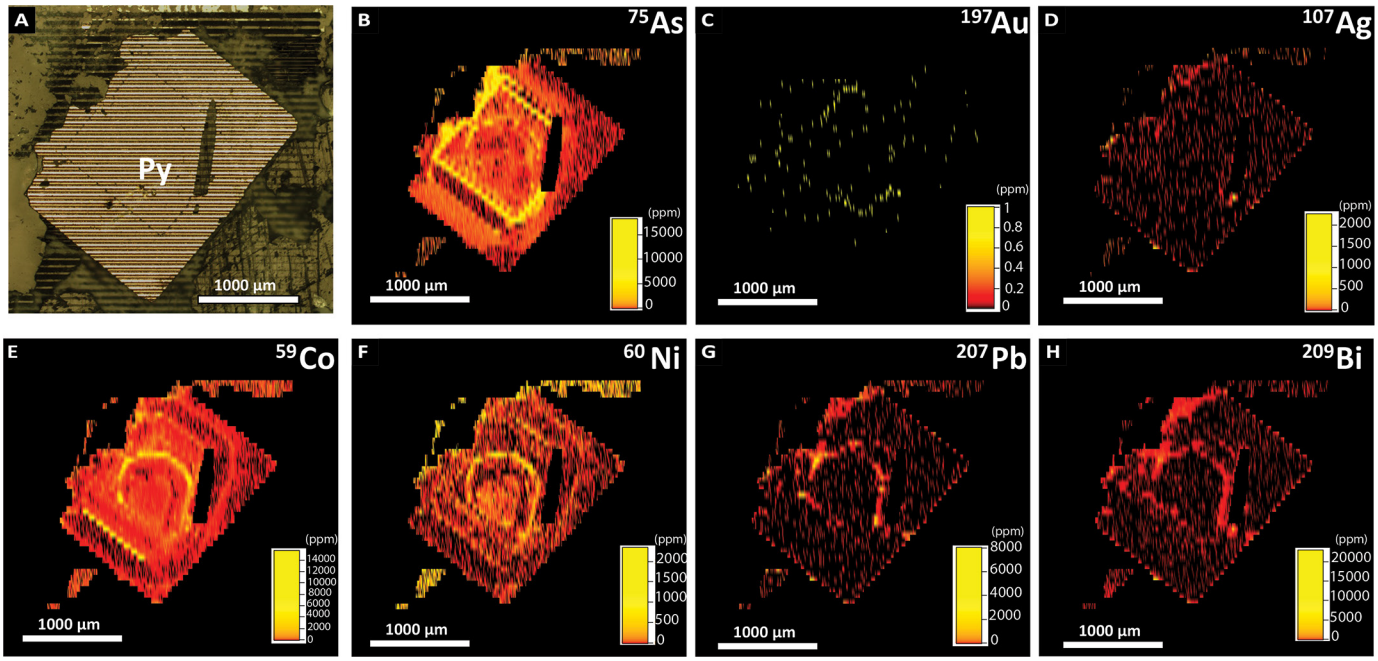

Fig. 14. LA-ICP-MS trace elements maps (in ppm) of a zoned euhedral pyrite (Py) grain from the gray-green sericite alteration zone (drill core DDH386, sample 459). A) Reflected-light photograph of the analyzed pyrite grain. B) ^{75}As map. C) ^{197}Au map. D) ^{107}Ag map. E) ^{59}Co map. F) ^{60}Ni map. G) ^{207}Pb map. H) ^{209}Bi map. Results show a Co-Ni-Pb-Bi–rich core with an outer As-Au–rich band.

hundreds of parts per million up to ~1,000 ppm (Fig. 10). Also, Bi is high in bornite, ranging from 3.4 to 5,940 ppm, although the upper limit may suggest the presence of inclusions.

Previous studies have shown that bornite is a major host of Ag and Bi. Cook et al. (2011) reported mean Ag concentrations ranging from hundreds to thousands of parts per million in bornite from several types of deposits, including porphyry, skarn, and iron oxide copper-gold (IOCG). In addition, Reich et al. (2013b) also reported high Ag in bornite from the Mantos Blancos Cu deposit in northern Chile (81–649 ppm Ag). Bismuth concentrations are also significant in bornite from several deposit types, reaching in some cases >1 wt % (Cook et al., 2011). At Río Blanco, it is likely that both Ag and Bi were incorporated as structurally bound elements within the bornite structure, considering that most LA-ICP-MS analyses are inclusion free and Ag has a behavior similar to that of Cu during ablation; however, some mineral inclusions of Ag (and Bi) were also observed within bornite (App. 12). Substitutional mechanisms of Ag and Bi in bornite appear similar to those in chalcopyrite, with Ag and Bi substituting in Cu and Fe sites, respectively. However, more experimental and spectroscopic data are required to assess the mechanisms of Ag and Bi incorporation in bornite, including potential effects of temperature-dependent exsolution or phase separation (see Cook et al., 2011, for discussion).

The Ag concentration in bornite at Río Blanco increased during cooling, a trend that is opposed to that observed for Ag in chalcopyrite (Ag is preferentially concentrated in chalcopyrite from the early, high-temperature potassic alteration stage). This general pattern for bornite can be observed in an Ag versus Bi diagram (Fig. 16; Cook et al., 2011). Silver displays a positive correspondence with Bi, with almost all Ag/Bi ratios between 0.20 and 2.00, except for bornite associated with the background albite (tourmaline-specularite) alteration zone (Ag/Bi >40). Bornite from the two potassic subzones, biotite > K-feldspar and K-feldspar > biotite, have Ag/Bi ratios between 0.30 and 3.08, respectively, while bornite from the gray-green sericite (transitional) zone (gray-green sericite > K-feldspar-biotite) are characterized by ratios between 0.34 and 1.43. Finally, bornite from the gray-green sericite moderate alteration zone has Ag/Bi ratio between 0.19 and 0.25 (Fig. 16). We interpret this trend as due to changes in Ag and Bi incorporation into bornite resulting from cooling, as suggested by Cook et al. (2011) based on mineralogical observations and fluid inclusion data assessment. High-temperature bornite from the potassic zone has higher Ag/Bi ratios, while lower Ag/Bi ratios characterize bornite from the lower-temperature alteration zone (e.g., gray-green sericite moderate alteration zone) (Fig. 16).

Among sulfides, pyrite presents the lowest Ag concentrations at the Río Blanco PCD (up to ~50 ppm; Fig. 11; App. 13), although concentrations of other critical elements can be of significance (e.g., Co, Ni, and Au; see Fig. 11A). This is in agreement with most published studies on pyrite geochemistry, which show that Ag is not preferentially incorporated into pyrite, in contrast to Au that is related to the As concentration (Reich et al., 2005, 2013a; Deditius et al., 2011, 2014). At Río Blanco, few Ag-bearing inclusions were observed in pyrite; consequently, and considering the low detected Ag concentrations, pyrite is not considered a significant Ag host in this deposit. However, there are Ag-As-Cu–rich bands on the edges of pyrite grains from the quartz-sericite zone (Fig. 13). The irregularly shaped pyrite morphology and colloform-like, fine (≤10 μm) overgrowths suggest a late dissolution-repre-

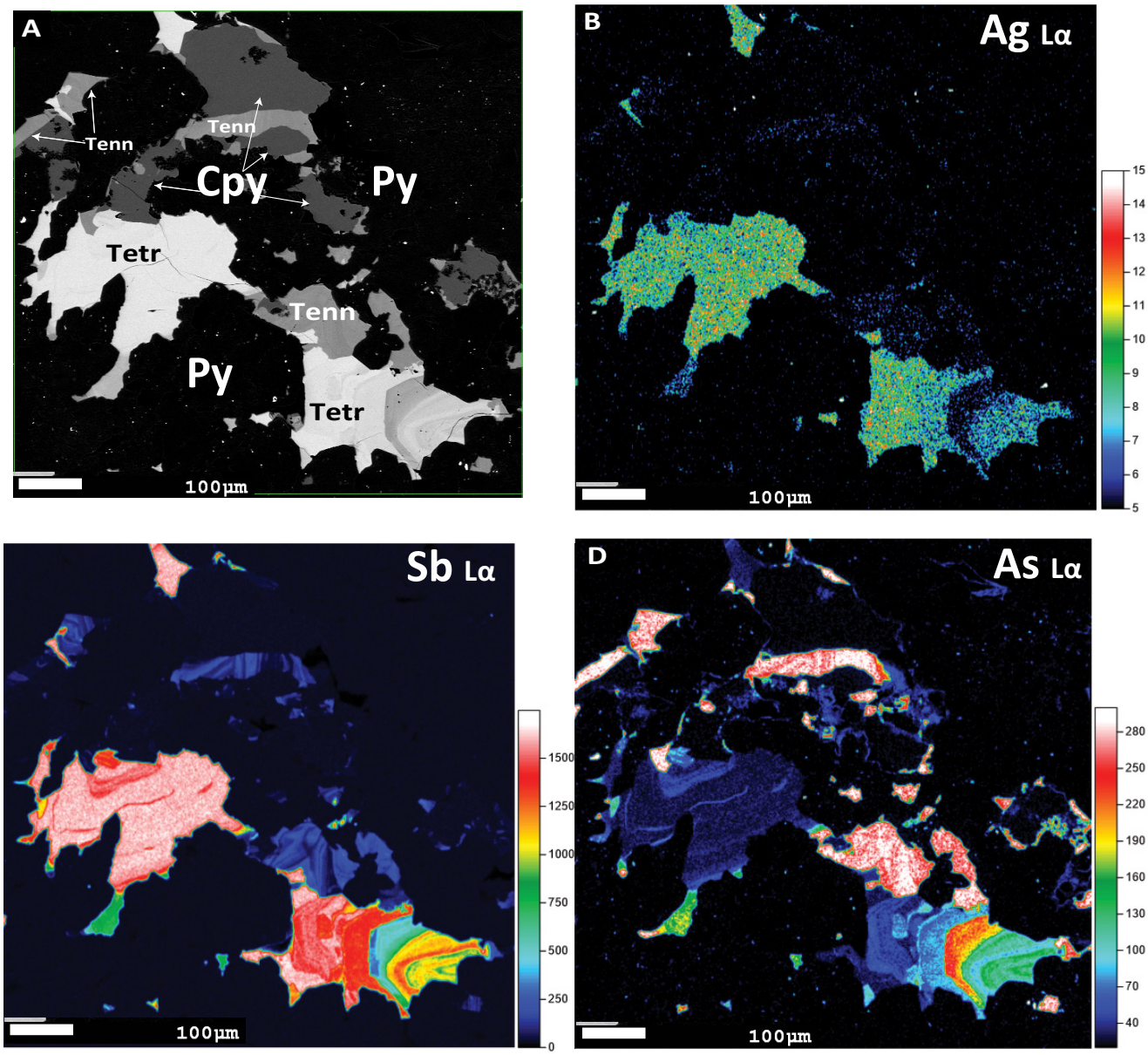

Fig. 15. BSE image and qualitative WDS X-ray maps of a tennantite-tetrahedrite-pyrite-chalcopyrite assemblage from the quartz-sericite alteration zone (drill core TSS-62, sample 288.5). A) BSE image of pyrite-chalcopyrite-tennantite-tetrahedrite. B) Ag (Lα) map. C) Sb (Lα) map. D) As (Lα) map. A color scale bar, which represents the intensity of the detector signal, is shown for each WDS map. Abbreviations: Cpy = chalcopyrite, Py = pyrite, Tenn = tennantite, Tetr = tetrahedrite.

cipitation event that may be synchronous with the deposition of Cu sulfosalts. High Ag-As-Cu concentrations in the bands negatively correlate with Fe and S contents (Fig. 13B-D), suggesting replacement in structural sites of pyrite (Reich et al., 2005; Deditius et al., 2014, and references therein).

Despite being largely restricted to the late stages of hydrothermal evolution at Río Blanco, enargite, tennantite, and tetrahedrite are the main Ag hosts, reaching up to weight percent levels (Fig. 12; App. 13). The scatterplot of Ag versus Sb shows increasing Ag with increasing Sb, from the Sb-poor enargite to the Sb-rich tetrahedrite (Fig. 17A), as well as a positive correlation with Cd, Co, Bi, and Hg (Fig. 17A-E). In contrast, Ag versus Pb is negatively correlated (Fig. 17F). The fahlore species that are close to the Sb-rich end-member tetrahedrite tend to incorporate more Ag than tennantite (e.g., Wu and Petersen, 1977; Sack and Loucks, 1985; Petersen et al., 1990; Moëlo et al., 2008; Repstock et al., 2016; George et al., 2017; Li et al., 2019). Fahlore-group minerals are complex sulfosalts that belong to the tetrahedrite isotypic series with a crystal-chemical formula $(Cu,Ag)_{10}(Fe,Zn,Hg,Cu)_2(As,Sb)_4S_{13}$, where Ag correlates with Sb but shows little relation to As (Repstock et al., 2016). In Ag-bearing fahlores, including Ag-bearing tetrahedrite ($Cu_6[Cu_4(Fe,Zn)_2]Sb_4S_{13}$) and tennantite ($Cu_6[Cu_4(Fe,Zn)_2]As_4S_{13}$), silver substitutes for Cu in the structure (Repstock et al., 2016; Li et al., 2019). Besides Ag, tetrahedrite-tennantite can incorporate a wide range of

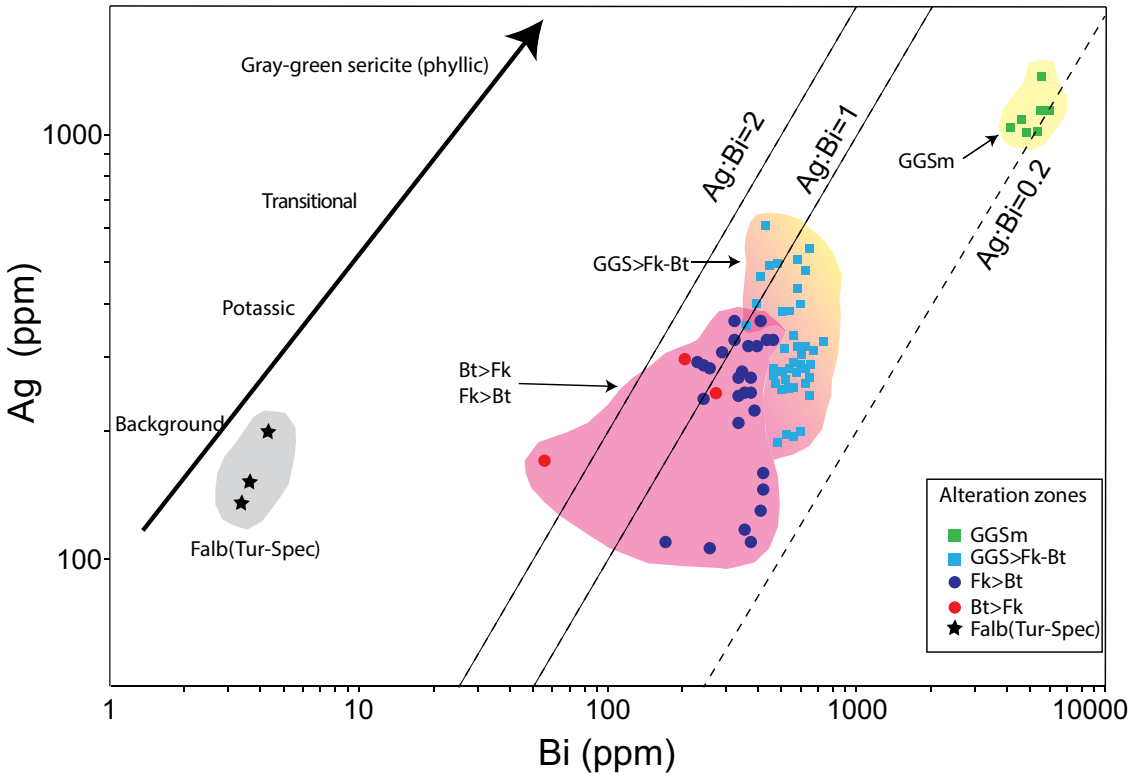

Fig. 16. Ag versus Bi scatterplot for bornite from the Río Blanco deposit (LA-ICP-MS data). Data are plotted in parts per million (ppm) on a logarithmic scale. Background albite (tourmaline-specularite) (Falb [Tur-Spec]) in gray, potassic alteration (biotite > K-feldspar [Bt > Fk]; K-feldspar > biotite [Fk > Bt]) in purple, transitional zone (gray-green sericite > K-feldspar-biotite [GGS > Fk-Bt]) between yellow and purple, and moderate gray-green sericite (GGSm) in yellow. Dashed lines represent different Ag/Bi ratios (0.2, 1.0, and 2.0). The data show a consistent trend of increasing Ag and Bi concentrations in bornite from the background potassic (higher T°) to the gray-green sericite (lower T°) stages.

trace elements including Zn, Cd, Hg, Bi, and In, among others (George et al., 2017). Enargite, on the other hand, can contain up to weight percent levels of Sb and Pb, while other elements such as Ag, Bi, Se, Te, Ag, and Zn occur at variable concentrations, in some cases exceeding 0.1 wt % (Deyell and Hedenquist, 2011).

At Río Blanco, Cu sulfosalts incorporated Ag (and other trace elements) during late-stage alteration. The tetrahedrite series contains Ag, as well being the main host of Sb and As in the deposit. The trace element concentrations of sulfides that formed during the late stages of white-mica alteration (i.e., pyrite, chalcopyrite, and minor bornite) indicate that tetrahedrite-tennantite is a primary host of Ag at Río Blanco, as well as elements such Bi, Cd, Pb, and Hg. In contrast, tetrahedrite-tennantite is a poor host for the critical metals In, Se, Te, or Au, all of which prefer to partition into other sulfides. Based on experimental and empirical studies (e.g., Klünder et al., 2003; Golebiowska et al., 2012), Bi-poor tennantite is generally interpreted as crystallizing at low temperatures (<200°C), with the most Bi-rich varieties crystallizing between 230°and 300°C (George et al., 2017).

Silver mineralization events at Río Blanco

Bulk-rock geochemical data and sulfide and sulfosalt mineral chemistry, discussed in the previous section, indicate that enrichment in Ag is coupled with the main hydrothermal alteration and Cu-Mo mineralization stages of the Río Blanco porphyry copper deposit (Fig. 4D). Based on published geochronology (Mathur et al., 2001; Frikken, 2004; Deckart et al., 2005, 2013; Hermosilla, 2015), we propose three main Ag mineralization events at Río Blanco, associated with the potassic, gray-green sericite, and quartz-sericite alteration stages (Fig. 18).

The earliest, relatively minor, Ag mineralization event at Río Blanco was related to the potassic alteration stage, first represented by early biotite and transitional-type veinlets, with mainly chalcopyrite and bornite (Fig. 18). Silver mineralization during this stage was dominantly hosted by Cu-Fe sulfides, which constitute the main Cu ores at Río Blanco. The bulk of Ag is predominantly hosted in solid solution within the structure of chalcopyrite and bornite (Figs. 9, 10), although some Ag is related to the occurrence of Ag-bearing micro- to nanosized mineral inclusions (Fig. 8; App. 12). In some cases, these inclusions can be associated with other critical metal particles, such Au or Pd (Crespo et al., 2018). This early potassic event was associated with the intrusion of the quartz monzonite porphyry (~7.05–6.48 Ma), the formation of the tourmaline and rock-flour breccias, and Mo mineralization, dated at 6.26 ± 0.04 Ma by Re-Os geochronology (Mathur et al., 2001). The subsequent main potassic event was associated with multiple porphyry intrusions—quartz monzonite porphyry, feldspar porphyry, and Don Luis porphyry (U-Pb ages between ~6.1 and 5 Ma). Predominant sulfides in the main potassic event are chalcopyrite in A- and B-type vein-

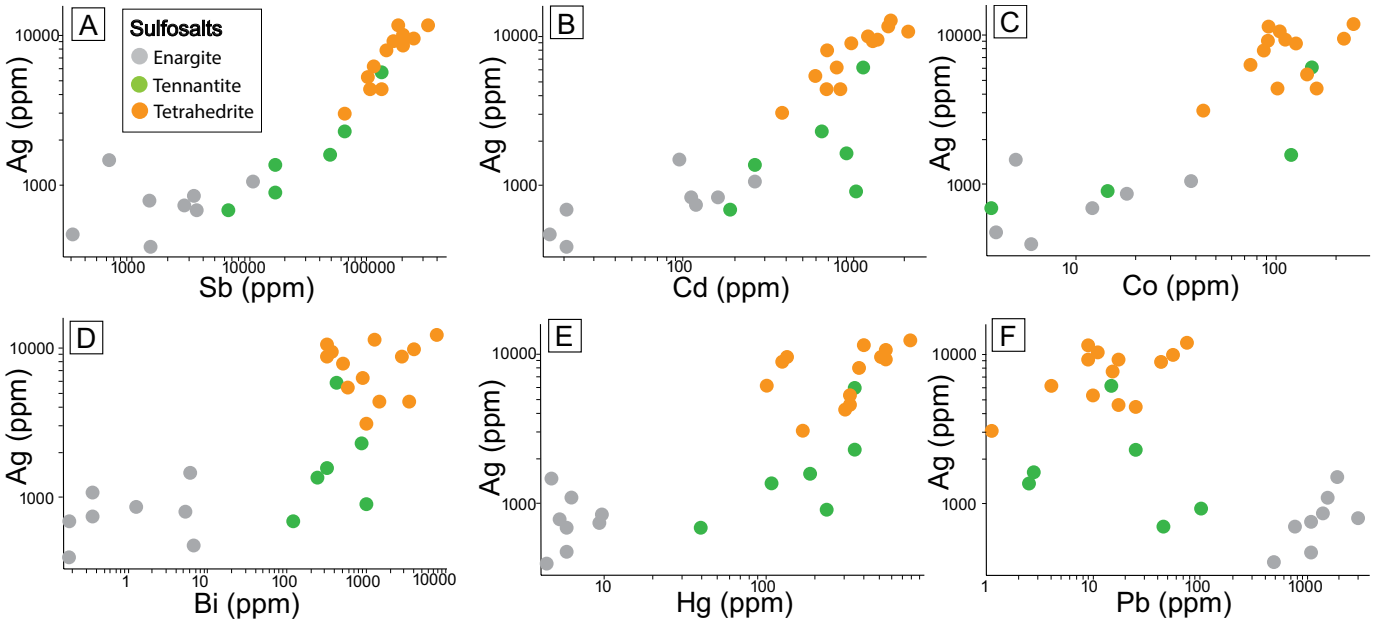

Fig. 17. Elemental concentration scatterplots for enargite, tennantite, and tetrahedrite (LA-ICP-MS data). A) Ag versus Sb. B) Ag versus Cd. C) Ag versus Co. D) Ag versus Bi. E) Ag versus Hg. F) Ag versus Pb. Data are plotted in parts per million (ppm) on a logarithmic scale. Tetrahedrite contains the highest concentrations of Ag and associated elements with the exception of Pb, which is higher in enargite.

lets. These potassic events were related to the formation of the silicified K-feldspar breccia (Ar-Ar ages ~6.1–4.9 Ma) and punctuated by Cu-Mo mineralization dated by molybdenite Re-Os geochronology between ~6.2 and 4.9 Ma (Mathur et al., 2001; Deckart et al., 2013) (Fig. 18). Based on mineralogical associations in early biotite, early biotite transitional, and A- and B-type veinlets, the high-temperature potassic alteration events at Río Blanco occurred at temperatures between 450°and 650°C (Gustafson and Hunt, 1975; Frikken, 2004; Frikken et al., 2005; John et al., 2010; Toro et al., 2012).

The second Ag mineralization event at Río Blanco (Fig. 18) was related to the transitional Cu-Mo mineralization event, which is represented by the gray-green sericite alteration, where C-type veinlets are characteristic. Mineral assemblages point to transitional temperatures for this event, between potassic and sericitic (near 400°C), as reported for several porphyry Cu deposits (e.g., Skewes and Atkinson, 1985; Gustafson and Quiroga, 1995; Rusk et al., 2008). Silver is hosted by chalcopyrite, bornite, and to a lesser extent pyrite; the Ag concentrations of bornite are higher than bornite of the potassic alteration zone (Fig. 16). Bornite from this stage has the highest Ag and Bi concentration (Fig. 16). Similar to the first event, the dominant form of Ag is in solid solution, although Ag-bearing mineral inclusions are observed in chalcopyrite and bornite, as well as filling microveinlets in pyrite and chalcopyrite.

The final event of Ag mineralization corresponded to the late quartz-sericite alteration stage (Fig. 18), characterized by D- and E-type veinlets with pyrite-chalcopyrite and enargite-tennantite-tetrahedrite. This event was related to the formation of the hematite breccia and the rhyolitic chimney (~4.69 ± 0.23 and 4.92 ± 0.09 Ma, respectively; Deckart et al., 2005, 2013) and coincident with the final pulses of Cu mineralization at Río Blanco, between ~4.9 and 4.5 Ma. Estimated temperature conditions of this event range between ~350° and 450°C to less than 300°C, based on mineralogical associations in D- and E-type veinlets (Gustafson and Hunt, 1975; John et al., 2010). During this stage, Ag was incorporated in greater amounts into Cu sulfosalts and chalcopyrite and in lesser amounts in pyrite. Silver-bearing minerals are more abundant in association with quartz-sericite alteration, including acanthite, proustite, polybasite, and pearceite, either as mineral inclusions or filling cavities and microfractures.

Concluding Remarks

Whole-rock geochemical data, SEM and FE-SEM mineralogical observations, and EMPA and LA-ICP-MS analyses provide evidence that Ag is concentrated in sulfides and sulfosalts in the Río Blanco porphyry Cu-Mo deposit. Our data indicate that enrichment of Ag is not exclusively associated with the late stage of Cu sulfosalt mineralization. Rather, Ag is distributed throughout the deposit over both space and time, hosted by chalcopyrite, bornite, and pyrite. Silver and associated elements such as In, Bi, Sb, As, Cd, Pb, Zn, Hg, Co, Ni, Se, Te, Au, and Pd occur in Cu-Fe sulfides and Cu sulfosalts, increasing from the early, high-temperature potassic to the late, lower-temperature quartz-sericite stage. EMPA and LA-ICP-MS data indicate that Ag concentrations are at least an order of magnitude higher in bornite (inclusion-free bornite, avg 356 ppm) than in chalcopyrite (inclusion-free chalcopyrite, avg 2.4 ppm). Silver contents in Cu sulfosalts from the quartz-sericite stage are generally one order of magnitude higher than those measured in bornite, with the highest concentrations measured in tetrahedrite (avg 7,907 ppm), followed by tennantite (avg 2,148 ppm) and enargite (avg 820 ppm). Pyrite at Río Blanco has the lowest average Ag concentration (inclusion-free pyrite, avg 0.55 ppm).

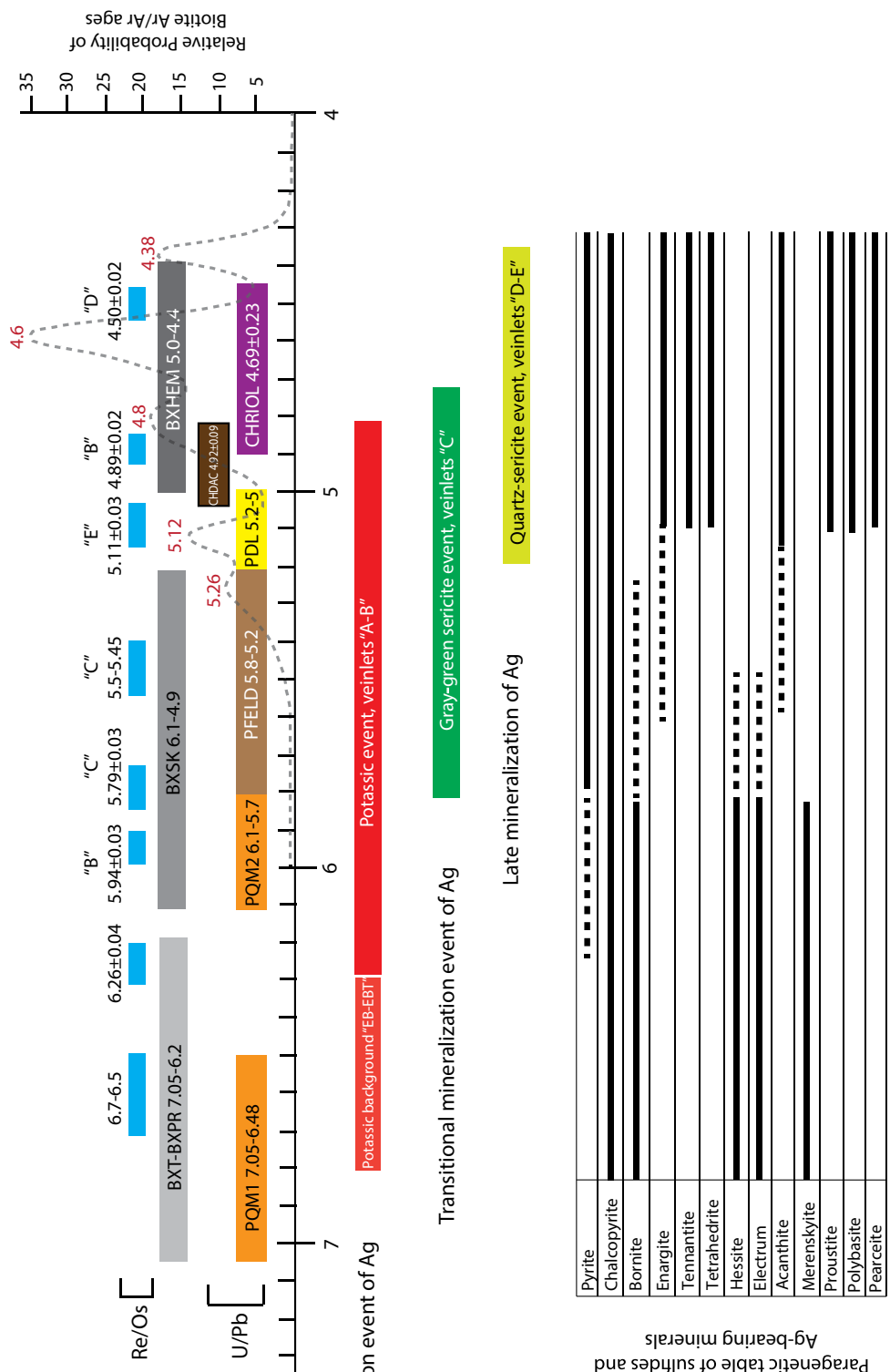

Fig. 18. Silver mineralization events at the Río Blanco PCD. Geochronological data are presented for intrusive units (U-Pb zircon ages), Cu-Mo mineralization (Re-Os molybdenite ages), and alteration ($^{40}Ar/^{39}Ar$). Data from Mathur et al. (2001), Deckart et al. (2005, 2013), and Hermosilla (2015). The earliest Ag mineralization event was related to the potassic alteration stage (early biotite-early biotite transitional-type veinlets [EB-EBT]) where the predominant sulfides are chalcopyrite and bornite. The second Ag mineralization stage was related to the (transitional) gray-green sericite alteration (C-type veinlets). Silver was partitioned preferentially into chalcopyrite, bornite, and to a lesser extent pyrite. The final stage of Ag mineralization corresponded to the late quartz-sericite alteration stage (D- and E-type veinlets) with pyrite-chalcopyrite and enargite-tennantite-tetrahedrite. A paragenetic sequence of sulfides, sulfosalts, and Ag-bearing minerals is also shown. Abbreviations: BXHEM = hematite breccia, BXSK = silicified K-feldspar breccia, BXT-BXPR = tourmaline breccia-rock-flour matrix breccia, CHDAC = dacite chimney, CHRIOL = rhyolite chimney, PFELD = feldspathic porphyry, PQM = quartz monzonite porphyry.

Silver mineralization events in the Río Blanco porphyry deposit are closely related to the main stages of hydrothermal alteration and Cu mineralization. Three Ag enrichment events were identified in the deposit:

1. Initial Ag introduction was related to the potassic alteration stage, with Ag hosted by chalcopyrite and bornite, predominantly as a structurally bound element (i.e., solid solution), although a minor part of the Ag tenor is attributable to micro- to nanosized inclusions of Ag-bearing minerals in chalcopyrite.
2. The second Ag mineralization event was related to the transitional Cu deposition event during the gray-green sericite alteration, with Ag increasingly incorporated in bornite rather than chalcopyrite, with minor amounts in pyrite. Silver is mainly in solid solution in the Cu-Fe sulfides, although increasing Ag-bearing microinclusions and microvein fillings were observed with paragenetic sequence.
3. The final Ag mineralization event was associated with the late quartz-sericite alteration stage. Silver occurs in sulfides and sulfosalts, particularly within the structure of tetrahedrite, tennantite, and enargite, but also as Ag-bearing minerals, which formed as a result of cooling.

From a genetic perspective, Ag was transported with Cu and other metals as chloride complexes in hydrothermal fluids, to be incorporated into sulfides and sulfosalts. Based on the predominant occurrence of Ag locked within Cu-Fe sulfides and Cu sulfosalts, we conclude that the hydrothermal fluids were largely undersaturated with respect to Ag minerals; however, local supersaturation occurred, particularly during the late quartz-sericite stage, with formation of Ag minerals.

At Río Blanco, Ag is typically associated with other critical elements of economic interest (John and Taylor, 2016). Among these, Bi and Se occur in the tens to hundreds of parts per million range in chalcopyrite, locally reaching thousands of parts per million in bornite and Cu sulfosalts (tennantite and tetrahedrite). Indium and Co, on the other hand, are ubiquitous in chalcopyrite and pyrite, respectively. Indium attains tens of parts per million in chalcopyrite, and Co can occur at the hundreds to 1,000 ppm range in pyrite. Tellurium occurs in all sulfides and also in sulfosalts, from a few parts per million to hundreds of parts per million. Gold is mostly present in pyrite (up to 10s of ppm), and Ge concentrations in the same range were detected in some pyrite grains. In addition, Pd-bearing particles hosted within bornite and chalcopyrite have been identified (Crespo et al., 2018), raising the possibility that PGEs will be found in sulfides from other Cu-Mo deposits.

Given the large size of the Río Blanco porphyry deposit and the large number of porphyry Cu systems in Chile and elsewhere, these deposits will become increasingly important suppliers of some critical metals (John and Taylor, 2016). For this to take place, detailed mineralogical studies similar to ours at Río Blanco are required to assess the potential of other porphyry deposits as sources of these commodities and to evaluate the economic recovery of the by-product elements.

Acknowledgments

This study was supported by Agencia Nacional de Investigacion y Desarrollo (ANID) through Millennium Science Initiative Program (NCN13_065). Additional support was provided by the Andean Geothermal Center of Excellence (CEGA), Fondo de Financiamiento de Centros de Investigación en Áreas Prioritarias (FONDAP) project 15090013. We thank CODELCO-Andina for providing data and access to the deposit and drill core database. The Center for Research in Nanotechnology and Advanced Materials (CIEN) of the Pontifícia Universidad Católica de Chile provided access to the FE-SEM used in this study, which was funded by Consejo Nacional de Investigación Científica y Tecnológica-Fondo de Equipamiento Científico y Tecnológico (CONICYT-FONDEQUIP) grant EQM150101. The LA-ICP-MS analytical work was supported by CONICYT-FONDEQUIP instrumentation grant EQM120098 and Centro de Excelencia en Geotermia de los Andes (CEGA). The Laboratorio de Microscopia Electrónica y Análisis por Rayos X (LAMARX) Laboratory of the Universidad Nacional de Córdoba, Argentina, is acknowledged for granting access to the electron microprobe facility. J.C. thanks the Iniciativa Científica Milenio for providing a Ph.D. scholarship and CODELCO Tech for providing a predoctoral Ph.D. fellowship. We thank Editor Larry Meinert and reviewers Jeff Hedenquist and Michael Gazley for their constructive and helpful comments.

REFERENCES

Arif, J., and Baker, T., 2004, Gold paragenesis and chemistry at Batu Hijau, Indonesia: Implications for gold-rich porphyry copper deposits: Mineralium Deposita, v. 39, p. 523–535.

Arndt, N.T., Fontboté, L., Hedenquist, J.W., Kesler, S.E., Thompson, J.F.H., and Wood, D.G., 2017, Future global mineral resources: Geochemical Perspectives, v. 6, p. 1–171.

Ballantyne, G.H., Smith, T.W., and Redmond, P.B., 1998, Distribution and mineralogy of gold and silver in the Bingham Canyon porphyry copper deposit, Utah: Society of Economic Geologists Guidebook Series, v. 29, p. 147–153.

Butler, I.B., and Nesbitt, R.W., 1999, Trace element distributions in the chalcopyrite wall of a black smoker chimney: Insights from laser ablation inductively coupled plasma mass spectrometry (LA-ICP-MS): Earth and Planetary Science Letters, v. 167, p. 335–345.

Cioacâ, M.E., Munteanu, M., Qi, L., and Costin, G., 2014, Trace element concentrations in porphyry copper deposits from Metaliferi Mountains, Romania: A reconnaissance study: Ore Geology Reviews, v. 63, p. 22–39.

CODELCO, 2018, División Andina—CODELCO, Corporación Nacional del Cobre: www.codelco.com/andina, accessed September 2018.

Cook, N.J., Ciobanu, C.L., Danyushevsky, L.V., and Gilbert, S., 2011, Minor and trace elements in bornite and associated Cu-(Fe) sulfides: A LA-ICP-MS study: Geochimica et Cosmochimica Acta, v. 75, p. 6473–6496.

Crespo, J., Reich, M., Barra, F., Verdugo, J.J., and Martinez, C., 2018, Critical metal particles in ore sulfides from the Río Blanco porphyry Cu-Mo deposit, Chile: Minerals, v. 8, p. 519.

Deckart, K., Clark, A.H., Celso, A.A., Ricardo, V.R., Bertens, A.N., Mortensen, J.K., and Fanning, M., 2005, Magmatic and hydrothermal chronology of the giant Río Blanco porphyry copper deposit, central Chile: Implications of an integrated U-Pb and $^{40}Ar/^{39}Ar$ database: Economic Geology, v. 100, p. 905–934.

Deckart, K., Clark, A., Cuadra, P., and Fanning, M., 2013, Refinement of the time-space evolution of the giant Mio-Pliocene Río Blanco-Los Bronces porphyry Cu-Mo cluster, central Chile: New U-Pb (SHRIMP II) and Re-Os geochronology and $^{40}Ar/^{39}Ar$ thermochronology data: Mineralium Deposita, v. 48, p. 57–79.

Deditius, A., Utsunomiya, Reich, M., Kesler, S.E., Ewing, R.C., Hough, R., and Walshe, E.J., 2011, Trace metal nanoparticles in pyrite: Ore Geology Reviews, v. 42, p. 32–46.

Deditius, A., Reich, M., Kesler, S.E., Utsunomiya, S., Chryssoulis, S., Walshe, J.L., Hough, R., and Ewing, R.C., 2014, The coupled geochemistry of Au and As in pyrite from hydrothermal ore deposits: Geochimica et Cosmochimica Acta, v. 140, p. 644–670.

Deyell, C.L., and Hedenquist, J.W., 2011, Trace element geochemistry of enargite in the Mankayan district, Philippines: Economic Geology, v. 106, p. 1465–1478.

Economou-Eliopoulos, M., 2005, Platinum-group element potential of porphyry deposits: Mineralogical Association of Canada Short Course Series, v. 35, p. 203–245.

Economou-Eliopoulos, M., and Eliopoulos, D.G., 1999, Palladium, platinum and gold concentration in porphyry copper systems of Greece and their genetic significance: Ore Geology Reviews, v. 16, p. 59–70.

Franchini, M., McFarlane, C., Maydagán, L., Reich, M., Lentz, D.R., Meinert, L., and Bouhier, V., 2015, Trace metals in pyrite and marcasite from the Agua Rica porphyry-high sulfidation epithermal deposit, Catamarca, Argentina: Textural features and metal zoning at the porphyry to epithermal transition: Ore Geology Reviews, v. 66, p. 366–387.

Frikken, P., 2004, Breccia-hosted copper-molybdenum mineralization at Río Blanco, Chile: Unpublished Ph.D. thesis, Hobart, Australia, University of Tasmania, 290 p.

Frikken, P.H., Cooke, D.R., Walshe, J.L., Archibald, D., Skarmeta, J., Serrano, L., and Vargas, R., 2005, Mineralogical and isotopic zonation in the Sur-Sur tourmaline breccia, Río Blanco-Los Bronces Cu-Mo deposit, Chile: Implications for ore genesis: Economic Geology, v. 100, p. 935–961.

Gena, K., Chiba, H., Kase, K., Nakashima, K., and Ishiyama, D., 2013, The Tiger sulfide chimney, Yonaguni Knoll IV hydrothermal field, southern Okinawa trough, Japan: The first reported occurrence of Pt-Cu-Fe–bearing bismuthinite and Sn-bearing chalcopyrite in an active seafloor hydrothermal system: Resource Geology, v. 63, p. 360–370.

Geological Society of America, 2013, Critical mineral resources: Position Statement, October 2013, www.geosociety.org/position/position23.htm.

George, L.L., Cook, N.J., and Ciobanu, C.L., 2016, Partitioning of trace elements in co-crystallized sphalerite-galena-chalcopyrite hydrothermal ores: Ore Geology Reviews, v. 77, p. 97–116.

——2017, Minor and trace elements in natural tetrahedrite-tennantite: Effects on element partitioning among base metal sulphides: Minerals, v. 7, p. 17.

George, L.L., Cook, N.J., Crowe, B.B.P., and Ciobanu, C.L., 2018, Trace elements in hydrothermal chalcopyrite: Mineralogical Magazine, v. 82, p. 59–88.

Golebiowska, B., Pieczka, A., and Parafiniuk, J., 2012, Substitution of Bi for Sb and As in minerals of the tetrahedrite series from Redziny, Lower Silesia, southwestern Poland: The Canadian Mineralogist, v. 50, p. 267–279.

Gustafson, L.B., and Hunt, J.P., 1975, The porphyry copper deposit at El Salvador, Chile: Economic Geology, v. 70, p. 857–912.

Gustafson, L.B., and Quiroga, J., 1995, Patterns of mineralization and alteration below the porphyry copper orebody at El Salvador, Chile: Economic Geology, v. 90, p. 2–16.

Harris, D.C., Cabri, L.J., and Nobiling, R., 1984, Silver-bearing chalcopyrite, a principal source of silver in the Izok Lake massive-sulfide deposit; confirmation by electron- and proton-microprobe analyses: The Canadian Mineralogist, v. 22, p. 493–498.

Hayes, S.M., and McCulloug, E.A., 2018, Critical minerals: A review of elemental trends in comprehensive criticality studies: Resources Policy, v. 59, p. 192–199.

Hermosilla, J., 2015, Caracterización geológica y cronológica de los eventos de intrusión/brechización y alteración/mineralización del yacimiento Río Blanco, Región Valparaiso, Chile: M.Sc. thesis, Antofagasta, Chile, Universidad Católica del Norte, p. 129–140.

Hollings, P., Cooke, D., and Clarke, A., 2005, Regional geochemistry of Tertiary igneous rocks in central Chile: Implications for the geodynamic environment of giant porphyry copper and epithermal gold mineralization: Economic Geology, v. 100, p. 887–904.

Irarrazaval, V., Sillitoe, R.H., Wilson, A., Toro, J.C., Robles, W., and Lyall, G., 2010, Discovery history of a giant, high-grade, hypogene porphyry copper-molybdenum deposit at Los Sulfatos, Los Bronces-Río Blanco district, central Chile: Society of Economic Geologists, Special Publication 15, p. 253–269.

Jochum, K.P., Willbold, M., Raczek, I., Stoll, B., and Herwig, K., 2005, Chemical characterization of the USGS reference glasses and BIR-1G using EPMA, ID-TIMS, ID-ICP-MS and LA-ICP-MS: Geostandards and Geoanalytical Research, v. 29, p. 285–302.

John, D.A., and Taylor, R.D., 2016, By-products of porphyry copper and molybdenum deposits: Reviews in Economic Geology, v. 18, p. 137–164.

John, D.A., Ayuso, R.A., Barton, M.D., Blakely, R.J., Bodnar, R.J., Dilles, J.H., Gray, F., Graybeal, F.T., Mars, J.C., McPhee, D.K., Seal, R.R., Taylor, R.D., and Vikre, P.G., 2010, Porphyry copper deposit model: U.S. Geological Survey, Scientific Investigations Report 2010-5070-B, 169 p.

Kesler, S.E., Chryssoulis, S.L., and Simon, G., 2002, Gold in porphyry copper deposits: Its abundance and fate: Ore Geology Reviews, v. 21, p. 103–124.

Kieft, K., and Damman, A.H., 1990, Indium-bearing chalcopyrite and sphalerite from the Gfisborn area, West Bergslagen, central Sweden: Mineralogical Magazine, v. 54, p. 109– 112.

Klünder, M.H., Karup-Moller, S., and Makovicky, E., 2003, Exploratory studies on substitutions in the tetrahedrite-tennantite solid solution series Part III. The solubility of bismuth in tetrahedrite-tennantite containing iron and zinc: Neues Jarbuch für Mineralogie Monatshefte, v. 2003, p. 153–175.

Li, W., Cook, N.J., Ciobanu, C.L., Xie, G., Wade, B.J., and Gilbert, S., 2019, Trace element distributions in (Cu)-Pb-Sb sulfosalts from the Gutaishan Au-Sb deposit, South China: Implications for formation of high fineness native gold: American Mineralogist, v. 104, p. 425–437.

Longerich, H.P., Jackson, S.E., and Günther, D., 1996, Laser ablation inductively coupled plasma mass spectrometric transient signal data acquisition and analyte concentration calculation: Journal of Analytical Atomic Spectrometry, v. 11, p. 899–904.

Mathur, R., Ruiz, J., and Munizaga, F., 2001, Insights into Andean metallogenesis from the perspective of Re-Os analyses of sulfides: South American Symposium on Isotope Geology, 3rd, Sociedad Geológica de Chile, Santiago, 2001, Extended Abstracts (CD-ROM), p. 500–503.

McFall, K.A., Naden, J., Roberts, S., Baker, T., Spratt, J., and McDonald, I., 2018, Platinum-group minerals in the Skouries Cu-Au (Pd, Pt, Te) porphyry deposit: Ore Geology Reviews, v. 99, p. 344–364.

Moëlo, Y., Makovicky, E., Mozgova, N.N., Jambor, J.L., Cook, N., Pring, A., Paar, W., Nickel, E.H., Graeser, S., Karup-Møller, S., et al., 2008, Sulfosalt systematics: A review. Report of the sulfosalt sub-committee of the IMA Commission on Ore Mineralogy: European Journal of Mineralogy, v. 20, p. 7–46.

Mpodozis, C., and Cornejo, P., 2012, Cenozoic tectonics and porphyry copper systems of the Chilean Andes: Society of Economic Geologists, Special Publication 16, p. 329–360.

Palenik, C.S., Utsunomiya, S., Reich, M., Kesler, S.E., and Ewing, R.C., 2004, "Invisible" gold revealed: Direct imaging of gold nanoparticles in a Carlin-type deposit: American Mineralogist, v. 89, p. 1359–1366.

Pašava, J., Vymazalova, A., Kosler, J., Koneev, R., Jukov, A.V., and Khalmatov, R.A., 2010, Platinum-group elements in ores from the Kalmakyr porphyry Cu-Au-Mo deposit, Uzbekistan: Bulk geochemical and laser ablation ICP-MS data: Mineralium Deposita, v. 45, p. 411–418.

Paton, C., Hellstrom, J., Paul, B., Woodhead, J., and Hergt, J., 2011, Iolite: Freeware for the visualization and processing of mass spectrometric data: Journal of Analytical Atomic Spectrometry, v. 26, p. 2508–2518.

Petersen, E.U., Petersen, U., and Hackbarth, C., 1990, Ore zoning and tetrahedrite compositional variation at Orcopampa, Peru: Economic Geology, v. 85, p. 1491–1503.

Piquer, J., Skarmeta, J., and Cooke, D.R., 2015, Structural evolution of the Río Blanco-Los Bronces District, Andes of central Chile: Controls on stratigraphy, magmatism, and mineralization: Economic Geology, v. 110, p. 1995–2023.

Piquer, J., Yáñez, G., Rivera, O., and Cooke, D., 2019, Long-lived crustal damage zones associated with fault intersections in the high Andes of central Chile: Andean Geology, v. 46, no. 2, p. 223–239, doi: 10.5027/andgeoV46n2-3106.

Reich, M., Kesler, S.E., Utsunomiya, S., Palenik, C.S., Chryssoulis, S., and Ewing, R.C., 2005, Solubility of gold in arsenian pyrite: Geochimica et Cosmochimica Acta, v. 69, p. 2781–2796.

Reich, M., Utsunomiya, S., Kesler, S.E., Wang, L.M., and Ewing, R.C., and Becker, U., 2006, Thermal behavior of metal nanoparticles in geologic materials: Geology, v. 34, p. 1033–1036.

Reich, M., Deditius, A., Chryssoulis, S., Li, J.W., Ma, C.Q., Parada, M.A., Barra, F., and Mittermayr, F., 2013a, Pyrite as a record of hydrothermal fluid evolution in a porphyry copper system: A SIMS/EMPA trace element study: Geochimica et Cosmochimica Acta, v. 104, p. 42–62.

Reich, M., Palacios, C., Barra, F., and Chryssoulis, S., 2013b, "Invisible" silver in chalcopyrite and bornite from the Mantos Blancos copper deposit: European Journal of Mineralogy, v. 25, p. 453–460.

Repstock, A., Voudouris, P., Zeug, M., Melfos, V., Zhai, M., Li, H., Kartal, T., and Matuszczak, J., 2016, Chemical composition and varieties of fahlore-group minerals from Oligocene mineralization in the Rhodope area, southern Bulgaria and northern Greece: Mineralogy and Petrology, v. 110, p. 103–123.

Román, N., Reich, M., Leisen, M., Morata, D., and Barra, F., 2019, Geochemical and micro-textural fingerprints of boiling in pyrite: Geochimica et Cosmochimica Acta, v. 246, p. 60–85.

Rubin, J.N., and Kyle, J.R., 1997, Precious metal mineralogy in porphyry-, skarn-, and replacement-type ore deposits of the Ertsberg (Gunung Bijih) district, Irian Jaya, Indonesia: Economic Geology, v. 92, p. 535–550.

Rusk, B.G., Reed, M.H., and Dilles, J.H., 2008, Fluid inclusion evidence for magmatic-hydrothermal fluid evolution in the porphyry copper-molybdenum deposit at Butte, Montana: Economic Geology, v. 103, p. 307–334.

Sack, R.O., and Loucks, R.R., 1985, Thermodynamic properties of tetrahedrite-tennantites; constraints on the interdependence of the Ag ⇔ Cu, Fe ⇔ Zn, Cu ⇔ Fe, and As ⇔ Sb exchange reactions: American Mineralogist, v. 70, p. 1270–1289.

Serrano, L., Vargas, R., Stambuk, V., Aguilar, C., Galeb, M., Holmgren, C., Contreras, A., Godoy, S., Vela, I., Skewes, A., and Stern, C., 1996, The late Miocene to early Pliocene Río Blanco-Los Bronces copper deposit, central Chilean Andes: Society of Economic Geologists, Special Publication 5, p. 119–130.

Sillitoe, R.H., 2010, Porphyry copper systems: Economic Geology, v. 105, p. 3–41.

Singer, D.A., Berger, V.I., and Moring, B.C., 2008, Porphyry copper deposits of the world—database and grade and tonnage models, 2008: U.S. Geological Survey, Open-File Report 2008-1155, 45 p., http://pubs.usgs.gov/of/2008/1155/.

Skewes, M.A., and Atkinson, W., Jr., 1985, Petrology of the early formed hydrothermal veins within the central potassic alteration zone of Los Pelambres porphyry copper deposit, Chile: Revista Geologica de Chile, no. 25–26, p. 39–56.

Stambuk, V., Blondel, J., and Serrano, L., 1982, Geología del Yacimiento Río Blanco: III Congreso Geológico Chileno, Concepción, Chile, November 8–14, 1982, Proceedings, p. 419–442.

Sykora, S., Cooke, D.R., Meffre, S., Stephanov, A.S., Gardner, K., Scott, R., Selley, D., and Harris, A.C., 2018, Evolution of pyrite trace element compositions from porphyry-style and epithermal conditions at the Lihir gold deposit: Implications for ore genesis and mineral processing: Economic Geology, v. 113, p. 193–208.

Tarkian, M., and Stribrny, B., 1999, Platinum-group elements in porphyry copper deposits: A reconnaissance study: Mineralogy and Petrology, v. 65, p. 161–183.

Thiele, R., 1980, Hoja Geológica de Santiago, Región Metropolitana, Chile: Servicio Nacional de Geología y Minería, Sernageomin, v. 29, p. 21.

Toro, J.C., Ortuzar, J., Zamorano, J., Cuadra, P., Hermosilla, J., and Sprohnle, C., 2012, Protracted magmatic-hydrothermal history of the Río Blanco-Los Bronces district, central Chile: Development of world's greatest known concentration of copper: Society of Economic Geologists, Special Publication 16, p. 105–126.

U.S. Department of Energy, 2011, Critical materials strategy: www.energy.gov/sites/prod/files/DOE_CMS2011_FINAL_Full.pdf, accessed June 10, 2018.

U.S. Geological Survey, 2019, Silver: Mineral Commodity Summaries, February, p. 150–151, https://prd-wret.s3-us-west2.amazonaws.com/assets/palladium/production/atoms/files/mcs-2019-silve.pdf.

Vargas, R., Gustafson, L., Vukasovic, M., Tidy, E., and Skewes, A., 1999, Ore breccias in the Río Blanco-Los Bronces porphyry copper deposit, Chile: Society of Economic Geologists, Special Publication 7, p. 281–298.

Vergara, M.M., and Latorre M., J., 1984, El complejo volcanico pliocenico de Río Blanco, Santiago: Revista Geológica de Chile, v. 22, p. 49–60, doi: 10.5027/andgeoV11n2-a05.

Warnaars, F.W., Holmgren, C., and Barassi, S., 1985, Porphyry copper and tourmaline breccias at Los Bronces-Río Blanco, Chile: Economic Geology, v. 80, p. 1544–1565.

Wei Goh, S., Buckley, A.N., Lamb, R.N., Rosenberg, R.A., and Moran, D., 2006, The oxidation states of copper and iron in mineral sulfides, and the oxides formed on initial exposure of chalcopyrite and bornite to air: Geochimica et Cosmochimica Acta, v. 70, p. 2210–2228.

Wilson, S.A., Ridley, W.I., and Koenig, A.E., 2002, Development of sulfide calibration standards for the laser ablation inductively-coupled plasma mass spectrometry technique: Journal of Analytical Atomic Spectrometry, v. 17, p. 406–409.

World Silver Survey, 2019, www.silver.fi/tiedostot/reports/190412_THE_SILVER_INSTITUTE_silver-survey-2019.pdf, accessed March 2019.

Wu, I., and Petersen, U., 1977, Geochemistry of tetrahedrite and mineral zoning at Casapalca, Peru: Economic Geology, v. 72, p. 993–1016.

Yáñez, G., and Rivera, O., 2019, Crustal dense blocks in the fore-arc and arc region of Chilean ranges and their role in the magma ascent and composition: Breaking paradigms in the Andean metallogeny: Journal of South American Earth Sciences, v. 93, p. 51–66, doi: 10.1016/j.jsames.2019.04.006.

Jorge Crespo holds a degree in geological engineering (B.Sc.) from the Central University of Ecuador and a Ph.D. degree from the University of Chile. He is a postdoctoral researcher in the Mining Engineering Department at Colorado School of Mines. He has more than 10 years of experience in the mining and exploration industry, largely focused in the Andes region of Ecuador, Chile, and Peru in porphyry Cu-Mo-Au and epithermal deposits. His research interests include the mineralogy, alteration, and geochemistry of hydrothermal ore deposits, trying to understand how metals concentrate and form large ore deposits in the crust.